Physics of Fluids ARTICLE pubs.aip.org/aip/pof

Ratcheting fluid pumps: Using generalized polynomial chaos expansions to assess pumping performance and sensitivity

Cite as: Phys. Fluids **36**, 121919 (2024); doi: 10.1063/5.0237403
Submitted: 4 September 2024 · Accepted: 27 November 2024 ·
Published Online: 18 December 2024

Zain Moin,[1] Laura A. Miller,[2] and Nicholas A. Battista[3,a)]

AFFILIATIONS

[1]Department of Biomedical Engineering, The College of New Jersey, 2000 Pennington Road, Ewing Township, New Jersey 08628, USA
[2]Department of Mathematics, University of Arizona, PO Box 210089, Tucson, Arizona 85721, USA
[3]Department of Mathematics and Statistics, The College of New Jersey, 2000 Pennington Road, Ewing Township, New Jersey 08628, USA

Note: This paper is part of the special topic, Fluids-Structure Interaction.

[a)]**Author to whom correspondence should be addressed:** battistn@tcnj.edu

ABSTRACT

A large diversity of fluid pumps is found throughout nature. The study of these pumps has provided insights into fundamental fluid dynamic processes and inspiration for the development of micro-fluid devices. Recent work by Thiria and Zhang [Appl. Phys. Lett. **106**, 054106 (2015)] demonstrated how a reciprocal, valveless pump with a geometric asymmetry could drive net fluid flow due to an impedance mismatch when the fluid moves in different directions. Their pump's geometry is reminiscent of the asymmetries seen in the chains of contractile chambers that form the insect heart and mammalian lymphangions. Inspired by these similarities, we further explored the role of such geometric asymmetry in driving bulk flow in a preferred direction. We used an open-source implementation of the immersed boundary method to solve the fluid-structure interaction problem of a viscous fluid moving through a sawtooth channel whose walls move up and down with a reciprocal motion. Using a machine learning approach based on generalized polynomial chaos expansions, we fully described the model's behavior over the target 3-dimensional design space, composed of input Reynolds numbers (Re_{in}), pumping frequencies, and duty cycles. Scaling studies showed that the pump is more effective at higher intermediate Re_{in}. Moreover, greater volumetric flow rates were observed for near extremal duty cycles, with higher duty cycles (longer contraction and shorter expansion phases) resulting in the highest bulk flow rates.

I. INTRODUCTION

Over the last millennium, nature has provided both inspiration for technology and insights into fundamental fluid dynamics.[2–4] One striking example of this is the animal heart. Leonardo da Vinci was perhaps the first to observe the vortices that formed in the sinuses of Valsalva and postulated that these low-pressure regions aid in valve closure.[5,6] This observation has inspired subsequent work in the formation of jets and vortices at intermediate Reynolds numbers[7–9] and has informed the design of artificial heart valves.[10] Similarly, the dynamics of the early embryonic heart have inspired innovations in the design of biohybrid and microfluidic pumps.[11–13] For example, it has been proposed that the early vertebrate heart is a dynamic suction pump,[14] and subsequent work has tested the usefulness of these pumps in generating unidirectional flow.[15,16]

Recent experimental, computational, and theoretical work has considered a type of valveless pump where fluid is transported using a ratcheting effect generated by a geometric asymmetry.[1,17–19] In this case, a reciprocal motion drives two asymmetric sawtooth structures facing each other. The structures form a corrugated fluid channel that generates different impedances when the fluid flows in different directions. Net flow is generated as a result of this impedance mismatch. As the fluid enters the channel from both ends during the expansion, the two opposing flows meet somewhere in the middle of the channel but with a bias that is due to the impedance mismatch. During contraction, the fluid flows out to both ends of the channel but with a similar directional bias. As the cycle repeats, the net transport of fluid is generated. The original design of this pump by Thiria and Zhang[1] was inspired by insect wings.[20]

The geometry of this ratcheting pump is reminiscent of the asymmetries observed in several biological pumps, including insect hearts and lymphangions (see Fig. 1). In the case of insect hearts, the pumping dorsal vessel consists of a chain of pumping chambers, divided by valves, that have a similar asymmetry,[21] see Fig. 1(a). Lymphangions, which are responsible for the active transport of lymph through the body, also consist of a chain of asymmetric pumping chambers that are separated by values,[22] see Fig. 1(b). Both the valves and the traveling peristaltic-like wave of contraction in these pumps contribute to the net transport of fluid.[22] However, the asymmetrical shape of the pumping chambers could further enhance the transport of fluid. Studying this mechanism in isolation might reveal how this morphology aids in the transport of lymph. Furthermore, bio-inspired innovation is and perhaps should be driven by loose interpretations of nature rather than the direct copying of it.[2,23,24] It is from this lens that we further explore the ratcheting fluid pump to gain insights into the mechanisms that may be responsible for transport in such biological pumps.

In this paper, we used the immersed boundary method to perform two-dimensional computational fluid dynamics (CFD) simulations of a ratcheting pump where the top and bottom walls were driven up and down in a reciprocal motion. We varied an input Reynolds number (Re) of the pump by changing the pumping frequency (which in turn changes the Strouhal number, St) and by varying the viscosity of the fluid (which does not change the Strouhal number). In addition, we varied the duty cycle (p) of the pump for a range of frequencies (f) and viscosities. We defined the duty cycle as the ratio of the pump's contraction period to the overall period of each actuation cycle. The volumetric flux over time and net average volumetric flux were calculated to assess the pump's performance across a parameter space composed of the Reynolds number (variable viscosity, fixed St), frequency (fixed Re, variable St), and duty cycle. In addition, fluid circulation in each chamber (tooth) of the pump was calculated to determine the relationship between vortex dynamics, parameter variations, and pump performance.

To understand how variations in scale (Re), pumping frequency (f), and duty cycle (p) affect pumping performance, we used a machine learning (ML) approach based on generalized polynomial chaos expansions (gPC) to help us reduce the number of simulations necessary to fully explore the 3D parameter space. In comparison with other surrogate ML techniques, such as neural networks, gPC provides the added benefit of an easier-to-interpret model function in the form of multivariate Legendre polynomials.[25,26] gPC expansions also require fewer training data for smaller dimensional parameter spaces.[27] Furthermore, gPC allows us to both predict scalar model output as

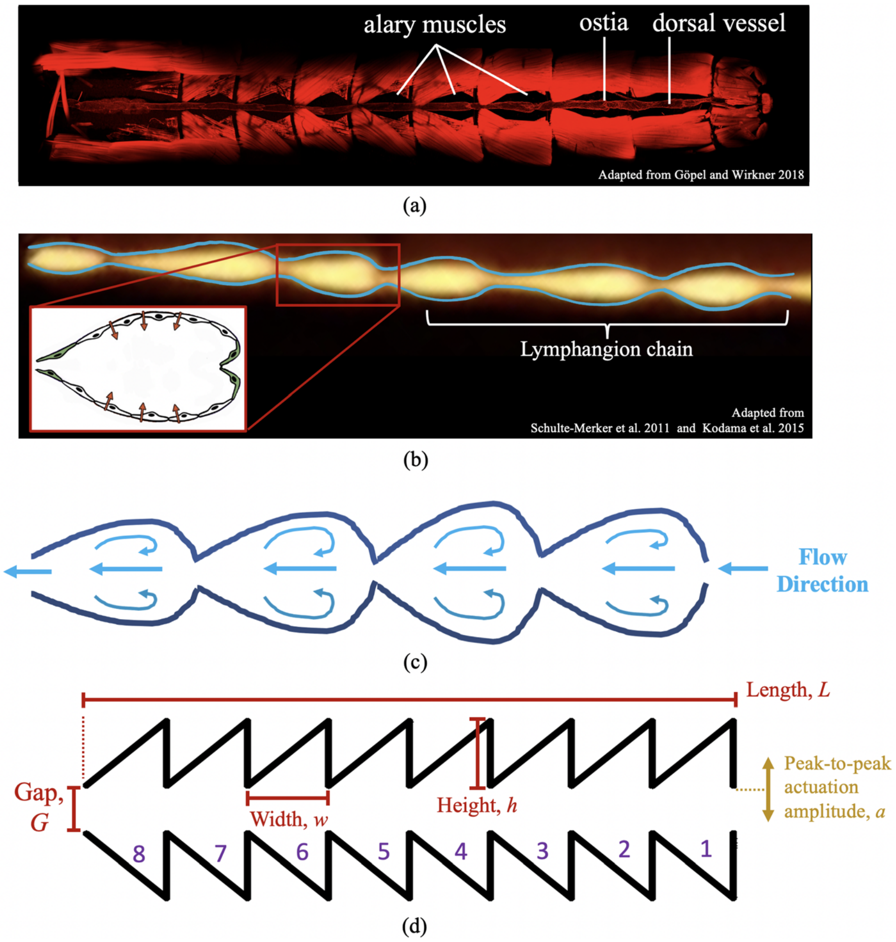

FIG. 1. (a) Ventral view of heart morphology of a mayfly (*Procloeon bifidum*). Adapted from Ref. 38. The dorsal vessel (tubular heart), ostia, and alary muscles are depicted. (b) Snapshot of multiple lymphangions taken from Media 1 of Kodama *et al.*[39] with an accompanying artist rendering of a single lymphangion. Adapted from Ref. 40. (d) Bioinspired fluid pump geometry to study asymmetric geometry effects on bulk flow properties, based on a further abstraction of (c) and inspired from the morphologies in (a) and (b). Reproduced with permission from Göpel and Wirkner, PLoS One **13**(9), e0201702 (2018). Copyright 2018 Author(s), licensed under a Creative Commons Attribution 4.0 International (CC BY) license. Reproduced with permission from Kodama *et al.*, Biomed. Opt. Express **6**, 124–134 (2015). Copyright 2015 Author(s), licensed under a Creative Commons Attribution 4.0 (CC BY) license. Reproduced with permission from Schulte-Merker *et al.*, J. Cell Biol. **193**, 607–618 (2011). Copyright 2011 Rockefeller University Press.

well as dynamic output metrics, with the added benefit of being able to assess global sensitivity to variations in uncertain parameters.[28–32] A system is deemed *sensitive* to an input parameter(s) if small variations in the parameter(s) result in substantial changes in its output. Global sensitivity analyses allowed us to quantify the impact of variations among the input parameters on the overall model output(s) in a holistic fashion,[33] as opposed to only local sensitivity measures.[34,35] Once the gPC was trained, validated, and tested, we could eliminate any further need for expensive simulation runs of the CFD model itself, to only needing to evaluate multivariate Legendre polynomials to predict pumping performance output metrics. Moreover, assessing global sensitivity through gPC provides the benefit of far fewer model evaluations than using low discrepancy sequences, such as Sobol' sequences,[36] to compute accurate Sobol' sensitivity indices.[26,29,37]

II. METHODS

The computational model followed the same geometry (size, shape, and scale) as that of the experimental apparatus of Thiria and Zhang,[1] but with only 8 *teeth* on each side of the pump rather than 11, see Fig. 1. Our simulations were performed with a fixed tooth width w and height h as in Ref. 1. However, while they varied both the initial gap between the top and bottom of the pump G and the peak-to-peak oscillation amplitude a, we held them fixed at $G = 0.325$ cm and $a = 0.337$ cm, respectively. This choice was deliberate to study other properties of this pumping system that were previously unexplored, namely how varying the duty cycle affects pumping performance in conjunction with variations in Reynolds number and/or pumping frequency. Note that the fixed geometric choices we made were previously shown to lead to effective pumping performance in Thiria and Zhang's experiment.[1]

We defined the *adjusted* input Reynolds number of the system to be

$$\mathrm{Re}_{in} = \frac{d \cdot (fa) \cdot L/G}{\nu}, \tag{1}$$

where ν is the fluid's kinematic viscosity, d is each tooth's width/height (recall $w = h$), f is the pumping frequency, G is the original gap between the top and bottom, and L is the total horizontal length of the pump. The product of fa can be viewed as a frequency-based characteristic velocity of the pumping system. This definition of Re_{in} is equivalent to the definition of the Reynolds number from Ref. 1. To initialize a simulation for a specific Reynolds number, an appropriate combination of ν and f must be chosen [see Eq. (1)]. Therefore, we will report an *adjusted* input Reynolds number (Re_{in}) for each ν and f combination. Note that we varied this input Reynolds number for a range of f to verify our computational model produced similar behavior to that observed by Thiria and Zhang[1] (see Sec. III B). A relationship between the selected f, ν, and Re_{in} is provided in Fig. 25 in Appendix D.

Similar to Thiria and Zhang,[1] we only actuated the top of the pump (the bottom remained fixed). However, unlike their work, we also varied the *duty cycle* of the actuation behavior. We defined the duty cycle p as the ratio of the total contraction time of the pump to the total period of each actuation cycle. Previous experimental work only investigated the case in which $p = 0.50$.[1] To study how asymmetric pumping kinematics affect the pump's performance, we chose duty cycles was between $0.2 \leq p \leq 0.8$, see Fig. 2. Varying both duty cycle and frequency may affect vortex formation and vortex interaction dynamics. This parameter space allowed us to more closely investigate how vortex dynamics, i.e., circulation, are largely responsible for the pump's performance. We used a piece-wise continuous sinusoidal stencil to prescribe the motion of the pump, i.e.,

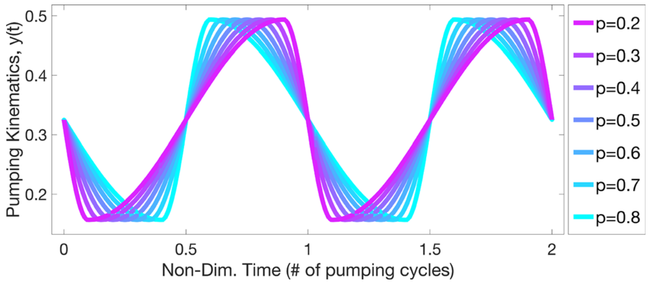

FIG. 2. Depiction of the vertical pumping motion given by Eq. (2) for a variety of duty cycles, *p*.

$$y_{top}(t) = \begin{cases} G - \dfrac{a}{2}\sin\left(2\pi \cdot t \cdot \dfrac{f_{con}}{2}\right), & t <= \dfrac{T_{con}}{2}, \\ G - \dfrac{a}{2}\cos\left(2\pi \cdot \left(t - \dfrac{T_{con}}{2}\right) \cdot \dfrac{f_{\exp}}{2}\right), & t <= \dfrac{T_{con}}{2} + T_{\exp}, \\ G + \dfrac{a}{2}\cos\left(2\pi \cdot \left(t - \dfrac{T_{con}}{2} - T_{\exp}\right) \cdot \dfrac{f_{con}}{2}\right), & t <= T. \end{cases} \tag{2}$$

The period of one pumping cycle was defined as $T = 1/f$. We defined temporal variables for the contraction and expansion phases of the pumping cycle using the duty cycle, p, i.e., $T_{con} = pT$ and $T_{\exp} = (1-p)T$, and hence $f_{con} = 1/T_{con}$ and $f_{\exp} = 1/T_{\exp}$. The time, t, was computed via modular arithmetic to stay within 1 pumping period, i.e., $t =$ "actual simulation time" $\mod T$. Figure 2 illustrates the prescribed pumping motion for a range of duty cycles p.

Table I provides the study's input parameters and pump's geometric parameters used in the study. The varied parameters were the

TABLE I. Pump's geometric parameters and model input parameter ranges across all the two-dimensional ratcheting fluid pump immersed boundary simulations.

Parameter	Variable	Units	Value
Total Simulation Time	$\mathcal{T}$	*Pumping cycles*	6
Pumping Frequency	f	Hz	[1,5]
Fluid Kinematic Viscosity	ν	cm^2/s	[0.017,2.47]
Input Reynolds number	Re_{in}	–	[10,300]
Duty cycle	p	–	[0.2,0.8]
Number of Teeth	N_T	–	8
Tooth Width	w	cm	0.63
Tooth Height	h	cm	0.63
Jaw Length	L	cm	5.04
Jaw Gap (resting)	G	cm	0.325
Actuation Amplitude	a	cm	0.337

fluid's kinematic viscosity (ν), pumping frequency (f), and the duty cycle (p). By changing both ν and f different fluid scales (Re_{in}) were considered. Although the size of the teeth (height, width) and the gap between jaws were based on parameters in Ref. 1, the number of teeth used in the study was 8 instead of 11.

As the simulations progressed, the instantaneous volumetric flow was spatially averaged across each end of the pump, separately, using the following formula:

$$VF_{R/L} = \overline{u}_{R/L}(t) \cdot Y(t), \tag{3}$$

where $\overline{u}_{R/L}(t)$ is the spatially averaged horizontal component of velocity and $Y(t)$ is the time-dependent distance between the top and bottom of the pump. The R/L designates either the volumetric flow over the right or left end of the pump, respectively. Across each simulation, 50-time points were saved during each pumping cycle, regardless of pumping frequency or duty cycle.

The overall *net* volumetric flow was computed as the difference between the left and right volumetric outflows. These data were then temporally averaged from the second to the sixth pumping cycle, $\overline{VF}$. The data were then non-dimensionalized in the following manner:

$$\overline{VF}_{ND} = \frac{\overline{VF}}{G \cdot (fa)}. \tag{4}$$

In addition to the flow velocities and volumetric flow rates, we defined the Strouhal number St and an output Reynolds number Re_{out} to be the following:

$$\mathrm{St} = \frac{G \cdot (fa)}{\overline{VF}} = \frac{1}{\overline{VF}_{ND}}, \tag{5}$$

$$\mathrm{Re}_{out} = \frac{d \cdot \frac{L}{G} \cdot \frac{\overline{VF}}{G}}{\nu} = \mathrm{Re}_{in} \cdot \overline{VF}_{ND} = \frac{\mathrm{Re}_{in}}{\mathrm{St}}. \tag{6}$$

Furthermore, fluid circulation was calculated across the bottom half of the pump, throughout the simulation. We computed the circulation within the gap and within each tooth separately. The circulation in the kth tooth was computed in the following manner:

$$\Gamma_k^n = \int_{\Omega_k} \omega^n dA \approx \sum_{i,j} \omega_{ij}^n dxdy, \tag{7}$$

where Ω_k is the area inside the kth tooth (as labeled by Fig. 1), and $\omega^n = \nabla \times \vec{u}^n$ is the fluid vorticity at time point n. Furthermore, dimensionless circulation was computed in the following manner:

$$\widetilde{\Gamma}_k^n = \frac{\Gamma_k^n}{f \cdot a \cdot G}. \tag{8}$$

The circulation within the gap was computed analogously. To decrease numerical errors due to sampling the data near the boundary, the area inside each tooth Ω_k was selected such that the grid cells used were five grid spatial widths from the pump geometry.

To solve the equations that govern this fluid-structure interaction (FSI) system, we used an open-source implementation of the immersed boundary method, `IB2d`.[41–43] Previously, the immersed boundary method (IB) has been applied to numerous valveless pump studies before, including peristaltic pumps,[44–48] dynamic suction pumps,[15,16,49–53] and electrodynamic suction pumps.[54,55] In this study, the pumping kinematics were fully prescribed, and the geometry was held nearly rigid, i.e., there were no flexible features. More details regarding IB and this model's implementation are provided in Appendix A. Furthermore, we also conducted a convergence study to ensure that the underlying physics was appropriately resolved (see Appendix B). The chosen grid resolution of $dx = L_x/N_x = 13.5/4608$ resulted in relative differences of less than 2.5% when compared to the highest resolution tested of $dx = 13.5/6912$ in volumetric flow rates.

A. Comparison with the experimental setup of Thiria and Zhang[1]

While the IB formalism allowed us to actuate the pump in the same manner as the experiment by Thiria and Zhang,[1] there were some notable differences between their experiment and our study. First, the modeling setup and experimental setup were slightly different (see Fig. 3). In our model, we only included the pump's geometry without any divider that separates the sides of the domain. Here, we measured the bulk flow properties directly out of both ends of the pump rather than out of a tank overflow tube, as in their experiment.[1] Second, gravity played a role in the experimental setup. In our study, however, we did not model gravitational effects. This was ignored in our model since the model setup and experimental setup were different as well as how we measured flow properties. Our model imposed periodic boundaries across every side of the computational domain, while the experiment had three physical boundaries (bottom, right, and left sides), on each side of the divider, with an air-water interface (free boundary) at the top of the tank. To the latter point, we defined the total flow out of the pump to be the difference between the flows from the left and right sides. Thus, we were able to measure direct flow properties without gravity playing an additional role. Third, although our simulations were performed in two dimensions, the experiment was inherently 3-dimensional. However, Thiria and Zhang suggested a two-dimensional representation would be sufficient to capture the necessary dynamics.[1] This idea was supported by their tank's depth being much larger than the average gap of the pump, i.e., $D \gg G$.

B. Generalized polynomial chaos expansions (gPC) surrogate model

A surrogate model based on generalized polynomial chaos (gPC) expansions was thoroughly trained, validated, and tested. gPCs are commonly used in uncertainty quantification as an elegant method to map the input parameter space to predicted output metrics (*quantities*

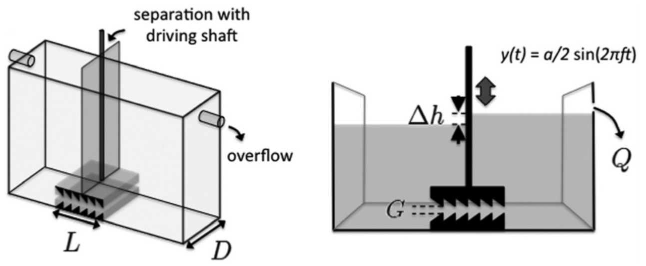

FIG. 3. Schematic of Thiria and Zhang's[1] experimental setup. Reproduced from Thiria and Zhang, Appl. Phys. Lett. **106**, 054106 (2015), with the permission of AIP Publishing.

of interest), with high accuracy.[26,37] In general, polynomial chaos expansions (PCE) cast square-integrable random functions in terms of orthogonal polynomials of the input parameters. That is, an appropriate Hilbert space is selected in which the model output (response surface) can be represented on that specific Hilbertian basis. Since quantifying variations in the model output due to fluctuations in the model input was of interest, the input parameters are thought to be random variables. Choosing the probability distribution functions to which the input parameters are sampled gives rise to a specific weight function for an inner product, thereby determining the specific family of orthogonal polynomials from an Askey scheme.[25] When the model output space is smooth, a polynomial chaos expansion can exhibit fast convergence to the response surface.[56] In this work, we sampled our input parameters from a uniform distribution, thus casting our PCE in terms of Legendre polynomials, i.e., the gPC's response surface was written as

$$S(\vec{\xi}) = \sum_{j=0}^{\mathcal{P}-1} c_j \Psi_j(\vec{\xi}), \tag{9}$$

where $\vec{\xi} = \{\text{Re}, f, p\}$, a set of input parameters, Ψ_j is a multidimensional Legendre polynomial, and $\mathcal{P}$ is the number of unknown coefficients $\{c_j\}_{j=0}^{\mathcal{P}-1}$, given by

$$\mathcal{P} = \binom{M+\mathcal{D}}{\mathcal{D}} = \frac{(M+\mathcal{D})!}{M!\mathcal{D}!}, \tag{10}$$

where $M = 3$ (the dimension of the parameter space) and $\mathcal{D}$ is the highest chosen degree of the multidimensional Legendre polynomial. The multidimensional Legendre polynomial can be decomposed into the product of individual one-dimensional Legendre polynomials, one for each input parameter. For example, we decomposed the jth multidimensional Legendre polynomial from (9) in the following manner:

$$\Psi_j(\xi_1, \xi_2, \xi_3, \ldots, \xi_M) = \prod_{n=1}^{M} \mathcal{L}_n^{\ell_n}(\xi_n), \tag{11}$$

where ℓ_n was the specific order of the one-dimensional Legendre polynomial $\mathcal{L}_n$ such that the cumulative sum of all of those individual orders was less than or equal to $\mathcal{D}$, i.e.,

$$\sum_{n=1}^{M} \ell_n \leq \mathcal{D}.$$

Note that we constructed our gPC using an order of $\mathcal{D} = 7$. This choice was made due to preliminary work suggesting that our pumping model's output was sufficiently smooth and did not demonstrate a high degree of nonlinear behavior across the input parameter space.

The gPC alleviated the massive computational expense associated with having to perform thousands of FSI simulations of our pumping system to thoroughly explore a target parameter space consisting of three parameters and perform global sensitivity analysis. In total, we ran 540 FSI simulations, 240 of which were used to generate our training dataset, with the remaining to be used as test data. For the training data, the 3D parameter space was sampled at points where the $(\mathcal{D}+1)st$ Legendre polynomials are zero

$$\mathcal{L}^{\mathcal{D}+1}(x) = 0 \quad \text{where } x \in [-1, 1].$$

Therefore, for each dimension of the 3-dimensional space, there were $\mathcal{D}+1 = 8$ possible roots. We then cast those points through linear transformations into the desired interval for each input parameter, i.e., $\text{Re} \in [10, 300]$, $f \in [1, 5]$, and $p \in [0.2, 0.8]$. Thus, the entire sampled space consisted of $8^3 = 512$ total parameter combinations, i.e., 512 specific combinations of three parameters. We sub-sampled these possible combinations down to 240 following the empirical rules suggested in Refs. 29 and 57, i.e., to sub-sample: only use a total of $N = (M-1)\mathcal{P}$ sampled points in your training set and determine those points by choosing the combinations of roots that are *closest to the origin*. They observed that sampling more points did not yield more accurate results.[29,57] However, it is been proposed that the fundamental aspect regarding what the overall number of sampled points should be is that when solving for the coefficients, the over-determined linear system should have rank at least equal to the total number of terms in the expansion, $\mathcal{P}$[29,30,58] (see later discussion on computing the coefficients). Note that parameter space sampling is still an active area of research.[59] To generate an independent test dataset, we elected to use a Sobol' sequence of dimension 3 with 300 total unique selections to sample the 3D parameter space.[36] This was a deliberate choice to ensure that we (1) produced an unbiased test dataset using a different sampling strategy than the training data, and (2) maximized representation across the entire parameter space while minimizing the possibility of sampling dense patches within the space (such that could emerge from random sampling).[60]

The unknown coefficients were then determined through least squares minimization using the output quantities of interest from the training dataset, i.e., to find $\vec{c} = [c_0\, c_1 \cdots c_{\mathcal{P}-1}]$, we solved

$$\vec{c} = \min_{\tilde{\vec{c}}} \left\| \sum_{j=0}^{\mathcal{P}-1} \tilde{c}_j \psi_j(\vec{\xi}) - S(\vec{\xi}) \right\|_2, \tag{12}$$

where $\tilde{\vec{c}}$ converges to $\vec{c}$ through the minimization procedure and $S(\vec{\xi})$ was the true model output (the true simulation data itself). Note that Eq. (12) can be interpreted as an over-determined linear system, where least squares procedures can be used to find the best fit, i.e., computing the pseudo-inverse through singular value decomposition. Next, we validated that the gPC surrogate model was able to accurately recover the training data as well as the test datasets. The latter suggested that the gPC model was an accurate surrogate model for this study. Thus, it could be used to predict performance for parameter combinations not explicitly simulated with the full FSI model. Figure 4 provides the numerical pipeline of how data from `IB2d` simulations get used to train and test a gPC-surrogate.

C. gPC model validation

Once the coefficients of our gPC surrogate model were computed using (12), we validated the gPC expansion against the training dataset. That is, we ensured that the gPC was able to accurately recover the training output. We did this for both the dimensional and dimensionless volumetric flow data and circulation data in two different ways as follows.

1. *Temporally over time*: The coefficients found in (12) are time-dependent and computed across one pumping cycle. That pumping cycle was averaged across each pumping cycle, i.e., each individual time point in the pumping cycle was found by averaging each corresponding time point among all pumping cycles performed.
2. *Time-averaged metrics*: Relative errors were calculated between the averaged output metrics of the full FSI simulated training data and the gPC predicted values.

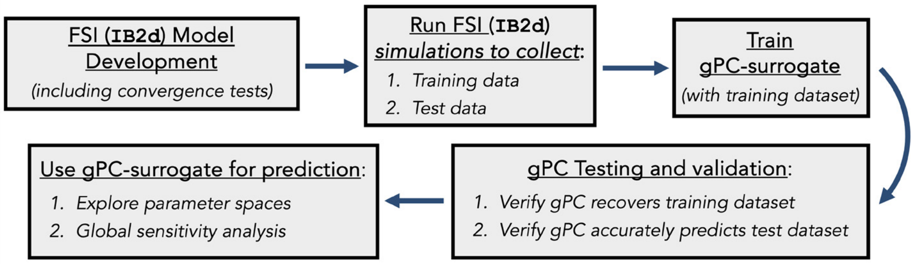

FIG. 4. Numerical pipeline of how data from `IB2d` simulations get used to train and test a gPC to use it as a surrogate model for prediction.

Note that the circulation data highlighted here was spatially averaged across each tooth and gap in the bottom half of the pump.

First, we computed the time-dependent coefficients of a gPC surrogate model to describe the waveforms of each output metric across one pumping cycle. We did this for a variety of cases in which we held two parameters constant and varied the third. We used the following parameters as the base case: $(\text{Re}_{in}, f, p) = (133.9, 3.37, 0.56)$. This case was chosen due to it being near the center of the parameter space. We saw qualitative agreement between all cases tested. Figure 5 provides comparative waveforms when the duty cycle is varied. The cases involving varying either Re_{in} or f are provided in Fig. 26 in Appendix D. This agreement suggested that our gPC surrogate model could be used to study dynamic output data.

However, most of this study focused on time-averaged output metrics. Therefore, we computed the relative error between the predicted time-averaged volumetric flow data and circulation data between the training dataset and the gPC predicted values for the same parameter combinations. Both qualitative and quantitative agreement was observed between the training data and gPC predicted quantities of interest. Figure 6 provides such comparisons for volumetric flow rates, while Fig. 27 in Appendix D gives a similar comparison for circulation. Overall, the validation statistics illustrate that the gPC surrogate can very accurately recover the training data's volumetric flow rates, showcasing less than 3.2% relative errors across all the training data, with an average error of 0.6%.

D. gPC model testing

We then tested our gPC model against our test dataset, i.e., data that were independent of our training dataset. We used a Sobol' sequence to sample the reduced 3D parameter subspace consisting of $\text{Re}_{in} \times f \times p = [15, 250] \times [1.25, 4.75] \times [0.25, 0.75]$, as mentioned at the end of Sec. II C. Similar to our validation step, we observed qualitative agreement between dynamical output quantities (see Fig. 7) and time-averaged scalar outputs [see Figs. 8(a) and 29(a) in Appendix D]. Moreover, the gPC yielded low relative errors between time-averaged scalar data [see Figs. 8(b) and 8(c)] between the gPC model and test data.

Figure 7 provides dimensionless volumetric flow and circulation over one pumping cycle for $\text{Re}_{in} = 125$, $f = 3.0$ Hz, and a variety of duty cycles. Cases involving variations of Reynolds number or pumping frequency are given in Fig. 28 in Appendix D. On the other hand, Fig. 8 presents relative error statistics for dimensionless time-averaged volumetric flow (a similar figure for dimensionless circulation is provided in Fig. 29 in Appendix D). Note that across all time-averaged output metrics, relative errors of less than 5% were achieved in $\gtrsim 94.3\%$ of all test cases considered, with an average relative error of 1.98%.

While it is common that test errors are greater than validation (training) errors in surrogate models,[61,62] we investigated where the largest relative errors in the test data stemmed from. We noticed that the cases that yielded such errors involved parameter combinations where one (or more) parameter values were very close to the edges of their respective ranges. We suspect that this was due to our sampling heuristic when choosing what parameters to use for our training data. Recall that the closest N parameter combinations to the center of the parameter space were chosen. As a result of this, cases involving extremal parameter values were not frequently used in the training.

E. gPC statistics and Sobol' sensitivity indices

Upon viewing the gPC expansion as the model's response surface, we computed its mean and overall variance directly from its coefficients [those found from Eq. (12)] and properties of the basis of the

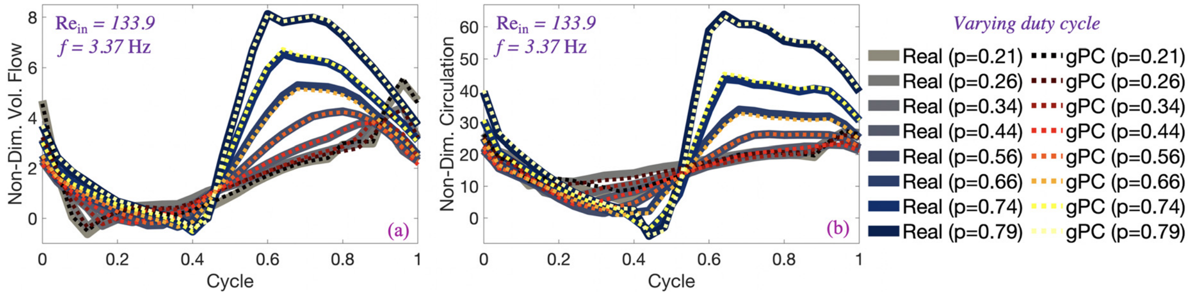

FIG. 5. Comparing the waveforms giving the dimensionless (a) volumetric flow rates and (b) circulation (averaged across each tooth and the gap in the bottom half of the jaw) over one pumping cycle between the training data (full FSI simulations) and the gPC surrogate model.

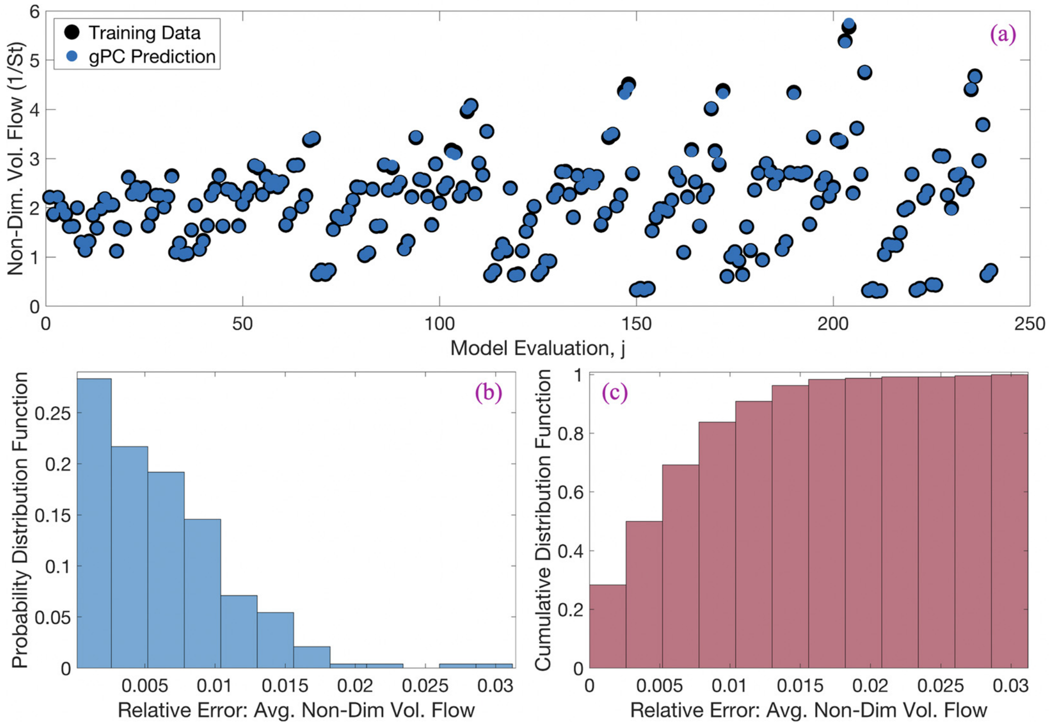

FIG. 6. (a) Qualitative comparison between the full FSI simulated training dataset involving dimensionless volumetric flow rates and the gPC-surrogate's predicted values. (b) Probability distribution function and (c) cumulative distribution function of the relative errors from those data in (a). Figure 27 in Appendix D provides a similar figure but for the circulation averaged across the bottom half of the pump.

probability space, here Legendre polynomials. The mean and variance were found to be

$$\overline{S} = E[S] = c_0, \tag{13}$$

$$D_{gPC} = \mathrm{Var}[S] = \sum_{j=0}^{\mathcal{P}-1} c_j^2 \cdot E\left[\Psi_j^2\right]. \tag{14}$$

Full derivations of the above two quantities are provided in Appendix C.

Furthermore, Sobol' sensitivity indices could be directly computed from the coefficients of the gPC itself.[29] Such sensitivity indices provide a measure of the global sensitivity of the model output to variations in its input.[33] The Sobol' functional decomposition (also called the *functional ANOVA decomposition*)[28,63] is a unique hierarchical expansion to decompose the variance in the model response. For a gPC expansion, we could write it in the following manner:

$$S(\vec{\xi}) = s_{000} + \sum_{i=1}^{3} \sum_{\vec{\alpha}\in\ell_{i_1}} s_{\vec{\alpha}}\psi_{\vec{\alpha}}(\xi_i) + \sum_{1\le i_1<i_2\le 3} \sum_{\vec{\alpha}\in\ell_{i_1,i_2}} s_{\vec{\alpha}}\psi_{\vec{\alpha}}(\xi_i,\xi_j) + \sum_{\vec{\alpha}\in\ell_{i_1,i_2,i_3}} s_{\vec{\alpha}}\psi_{\vec{\alpha}}(\xi_1,\xi_2,\xi_3), \tag{15}$$

where the coefficients $s_{\vec{\alpha}}$ were the same coefficients, $\vec{c}$, found in Eq. (12), but re-ordered, i.e.,

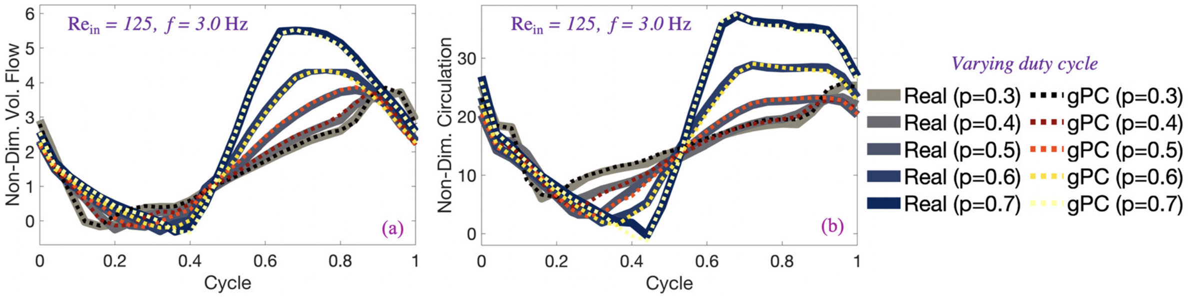

FIG. 7. Comparing the waveforms giving the dimensionless (a) volumetric flow rates and (b) circulation (averaged across each tooth in the bottom jaw) over one pumping cycle between the test data (full FSI simulations) and gPC surrogate model.

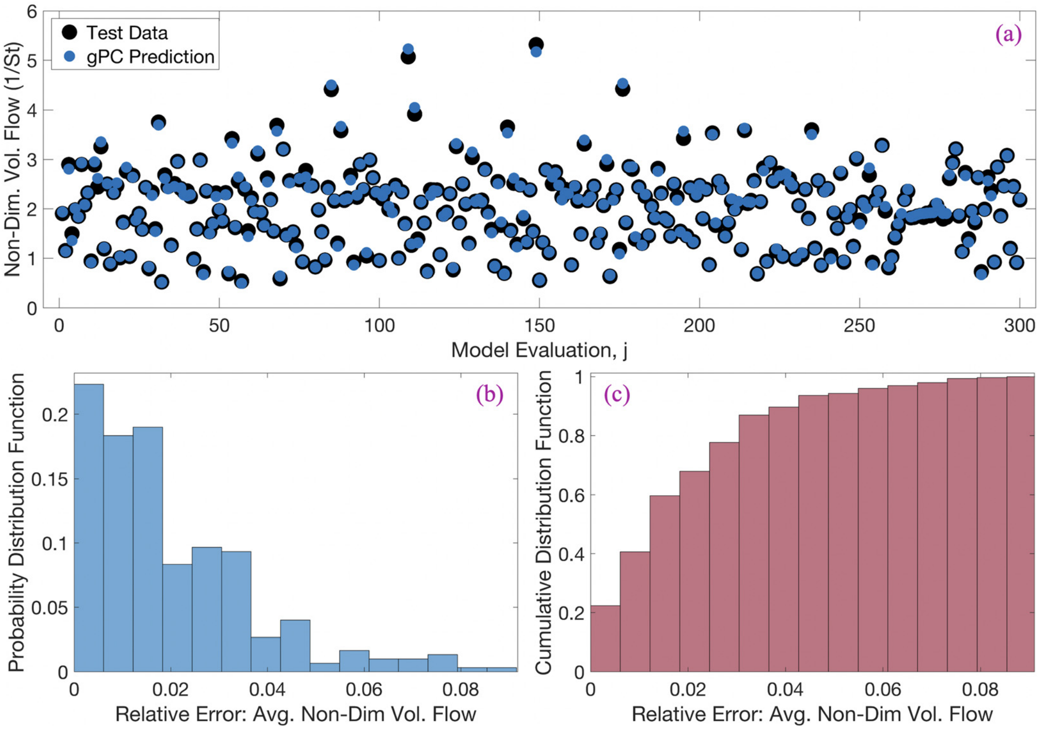

FIG. 8. (a) Qualitative comparison between the full FSI simulated test dataset involving dimensionless volumetric flow rates and the gPC-surrogate's predicted values. (b) Probability distribution function and (c) cumulative distribution function of the relative errors from those data in (a). Figure 29 in Appendix D provides a similar figure but for the circulation averaged across the bottom half of the pump.

$$S(\vec{\xi}) = \sum_{j=0}^{\mathcal{P}-1} c_j \psi_j(\vec{\xi}) = \sum_{j=0}^{\mathcal{P}-1} s_{\vec{\alpha}_j} \psi_{\vec{\alpha}_j}(\vec{\xi}) = \sum_{j=0}^{\mathcal{P}-1} s_{\vec{\alpha}_j} \prod_{i=1}^{3} \mathcal{L}_{\alpha_i}(\xi_i). \tag{16}$$

Moreover, we defined the indices, $\vec{\alpha}$ and ℓ_i in the following manner:

$$\ell_{i_1,\ldots,i_s} = \left\{ \vec{\alpha} : \begin{array}{lll} \alpha_k > 0 & \forall k = 1,2,\ldots,m & k \in (i_1, i_2, \ldots, i_s) \\ \alpha_j = 0 & \forall k = 1,2,\ldots,m & k \notin (i_1, i_2, \ldots, i_s) \end{array} \right\}. \tag{17}$$

The Sobol' sensitivity indices are a ratio of the variance that can be attributed to one (or more) parameters to the overall variance.[64] The higher the sensitivity index is, the more sensitive the model output is to that particular input parameter. The first-order Sobol' index quantifies the effect of varying a specific single parameter alone on the model's output. Meanwhile, the total-order index provides a measure of the total variance associated with that one parameter, even though others are varied, i.e., the total-order index is the sum of all the sensitivity indices involving that specific input parameter to D_{gPC}. For example, we calculated these indices for parameter ξ_1 in the following manner:

$$S_{\xi_1}^{\text{1st}} = \frac{1}{D_{gPC}} \sum_{\substack{\alpha_1 \neq 0 \\ \alpha_2 = \alpha_3 = 0}} s_{\vec{\alpha}}^2 \cdot E\left[\psi_{\vec{\alpha}}^2\right], \tag{18}$$

$$S_{\xi_1}^{\text{Tot}} = \frac{1}{D_{gPC}} \sum_{\substack{\alpha_1 \neq 0 \\ \alpha_2, \alpha_3 \\ (whatever)}} s_{\vec{\alpha}}^2 \cdot E\left[\psi_{\vec{\alpha}}^2\right]. \tag{19}$$

The indices associated with ξ_2 and ξ_3 followed similarly. We inferred the relative importance of higher-order parameter interactions by comparing the first-order and total-order indices. If there were substantial differences between both indices, it would suggest that the output was highly sensitive to varying a parameter in conjunction with one or more parameters. That is, higher-order interactions among parameters would be important. Note that higher-order indices can also be calculated directly from the $s_{\vec{\alpha}}$. However, as Sec. III F will describe, higher-order interactions did not contribute much to the overall variance in the model output in the 3D target input space explored here, see Figs. 39(b) and 40(b) in Appendix D.

III. RESULTS

A. Reciprocal motion can induce bulk transport

While we are interested in fully exploring how variations in fluid scale (Re_{in}), pumping frequency (f), and duty cycle (p) affect pumping performance, we will first briefly discuss how the sawtooth pump's reciprocal motion can induce net volumetric flow. It is the pump's geometric asymmetry that makes net volumetric flow possible. For example, Fig. 9 (Multimedia view) provides snapshots of tracer particles (and vorticity contours) for a $\mathrm{Re}_{in} = 150$ pump of $(\nu, f, p) = (0.0988, 3.0, 0.50)$. By the end of the fifth pumping cycle, the vast majority of the tracers were pushed toward the left side of the pump. Moreover, by the end of each contraction phase, distinct vortices formed within each tooth. Figure 10 (Multimedia view) provides colormaps of vorticity for the same case but across the first two

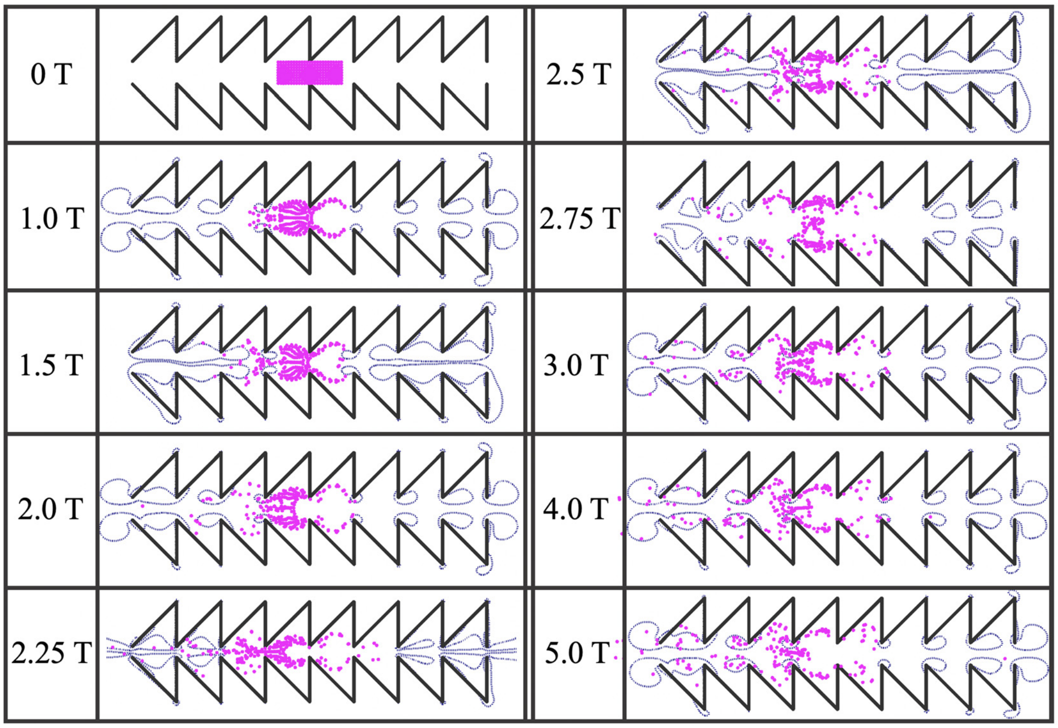

FIG. 9. Snapshots of tracers and vorticity contours for a $Re_{in} = 150$ case involving $\nu = 0.0988\,\mathrm{cm}^2/\mathrm{s}$, $f = 3.0\,\mathrm{Hz}$, and $p = 0.50$. Multimedia available online.

actuation cycles. Later, we will discuss the role of fluid circulation in the teeth to help achieve bulk transport. Notably, while Fig. 9 illustrates bulk flow moving left, Fig. 10 highlights that substantial backflow also occurs.

Time-dependent volumetric flows and overall net volumetric flows are provided in Fig. 11. When $p = 0.30$, large spikes in volumetric flow emerge during each short contraction phase out of the left and right of the pump, followed by smaller peaks (of opposite sign) during

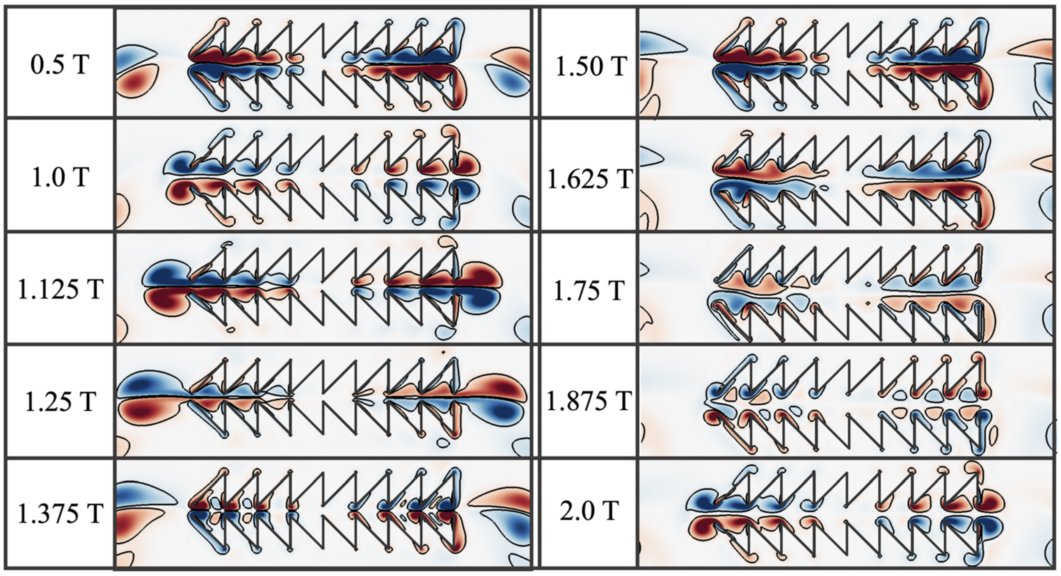

FIG. 10. Snapshops of vorticity for a $Re_{in} = 150$ case involving $\nu = 0.0988\,\mathrm{cm}^2/\mathrm{s}$, $f = 3.0\,\mathrm{Hz}$, and $p = 0.50$, across its second actuation cycle. Multimedia available online.

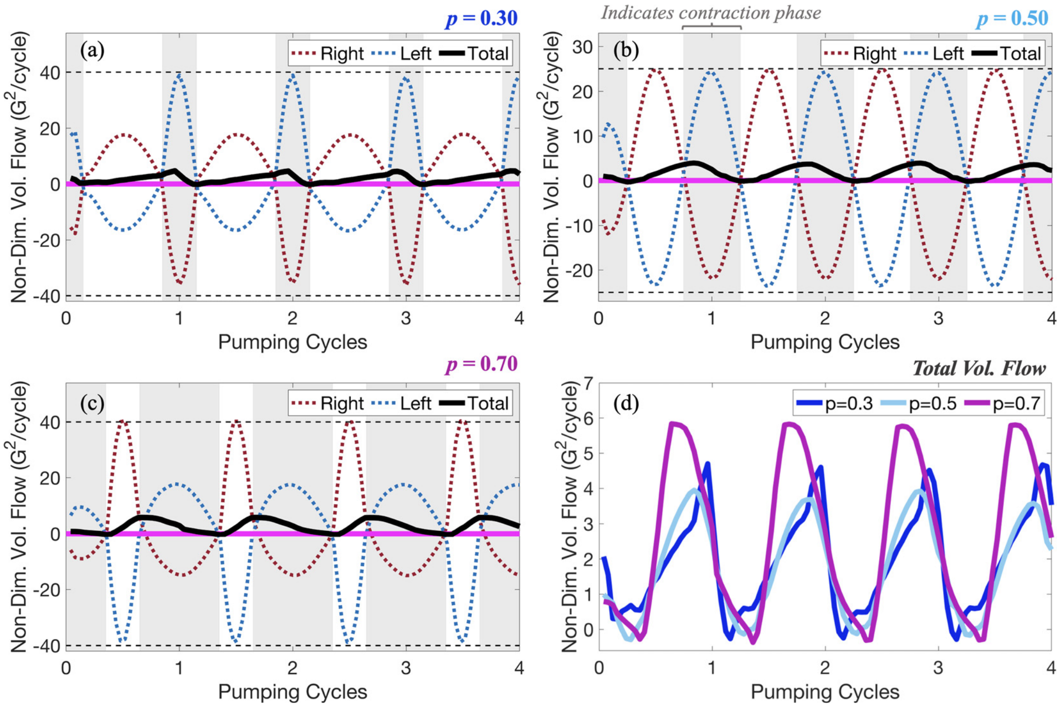

FIG. 11. Evolution of volumetric flow out of the left and right sides as well as the net volumetric flow of $\mathrm{Re}_{in} = 150$ cases composed of $\nu = 0.0988\,\mathrm{cm}^2/\mathrm{s}$ and $f = 3.0\,\mathrm{Hz}$ with duty cycles of (a) $p = 0.30$, (b) $p = 0.50$, and (c) $p = 0.70$. The shaded regions indicate the pump's contraction phase. The net volumetric flows from each of these cases are also provided in (d).

the subsequent expansion phase. As the peaks corresponding to flows out of the left side are larger, there is net volumetric flow toward the left, as previously shown by the tracers in Fig. 9. The thick black line gives the overall net volumetric flow. The data for duty cycle cases of $p = 0.50$ and $p = 0.70$ are also given in Fig. 11, for the same Re_{in} and f. The time-dependent volumetric flow waveforms between the $p = 0.30$ and $p = 0.70$ cases appear similar at first glance; however, there are noticeable differences. While they both exhibit two different peaks, one during contraction and one during expansion, their peaks are out of phase with one another. That is, in the case when $p = 0.30$, the taller peak occurs during contraction. On the other hand, when $p = 0.70$ the taller peak occurs during the expansion phase. Moreover, the shorter peak's waveform is also noticeably asymmetric in both cases and leans in different directions between both cases. The waveform in the $p = 0.50$ case maintains approximately the same shape throughout. Furthermore, each case's *net* volumetric flow waveform is different [Fig. 11(d)]. Comparing data for each case in Fig. 11(d) to their respective data in (a)–(c) shows that the maximal instantaneous net volumetric flow rate is only approximately $\sim$ 10%–15% of the maximum out of the left side only. This suggests a low bulk flow efficiency. Note that when the *net* volumetric flow is positive during the expansion phase, it implies that the pump is filling with more fluid from the right side than the left. A possible heuristic of this mechanism is briefly described as follows.

Consider the case involving a duty cycle of $p = 0.50$, i.e., equal contraction and expansion phases. Figure 12 (Multimedia view) depicts the vortex dynamics in the case of $\mathrm{Re}_{in} = 150$, $f = 3.0\,\mathrm{Hz}$, and $p = 0.50$. Immediately after expansion distinct clockwise (CW) and counterclockwise (CCW) vortex pairs are formed on the right side of the pump, while more complicated vortex interactions occur on the left side of the pump. The vortex pairs on the right side persist until just about halfway through contraction ($\sim 2.0T$). The spin of these vortices shows they act to resist backflow, i.e., flows out of the right side of the pump. Meanwhile, on the left side of the pump, vortices are formed that complement the flow out of the pump. Therefore, we suspect that geometric asymmetries enable vortex production that helps bias net flow toward a preferred direction. Moreover, we hypothesize that this mechanism can be boosted when combined with particular pumping kinematics, such as higher duty cycles [see Fig. 11(d)].

To investigate the mechanism that drives net volumetric flow, we chose a target 3D parameter space that included the fluid scale (an adjusted input Reynolds number, Re_{in}), actuation frequency (f), and duty cycle (p) and covered $\mathrm{Re}_{in} \times f \times p = [10, 300] \times [1, 5]\,\mathrm{Hz} \times [0.2, 0.8]$. To thoroughly explore this parameter space, an ML surrogate model, based upon generalized polynomial chaos expansions, was trained, validated, and tested. This allowed us to predict the pump's performance over a plethora of input parameter combinations in an inexpensive, rapid manner while maintaining high accuracy. Using such a surrogate model was particularly attractive given the computational cost of simulating the full FSI model, both in computational time and computational storage. For example, given `IB2d` is written in interpretative programing languages (MATLAB and Python), a simulation with a pumping frequency of 3 Hz, time step of $dt = 2.5 \times 10^{-5}$, $[N_x, N_y] = [4608, 1152]$, and for six pumping cycles required

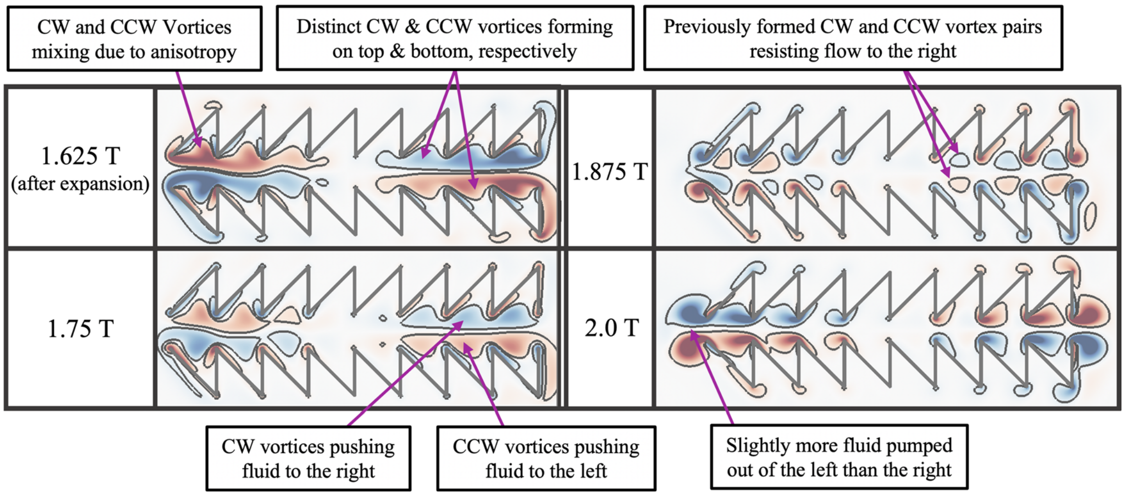

FIG. 12. Colormaps illustrating snapshots of vorticity for the case when $\mathrm{Re}_{in} = 150$, $f = 3.0\,\mathrm{Hz}$, and $p = 0.50$, during contraction in the second actuation cycle. Multimedia available online.

approximately 32 days of computational time on a 2.40 GHz Intel Skylake Gold processor with 192 Gb RAM memory.[65]

Ultimately, as the input Reynolds number, frequency, and duty cycle were varied, the pumping system exhibited nonlinear behavior. The remainder of this section will identify parameter combinations that led to higher net volumetric flow rates. We will also discuss the physical mechanism leading to bulk transport in Sec. III E and the pump's global sensitivity to parameters in Sec. III F.

B. Volumetric flow rates collapse to single curve for different actuation frequencies

Thiria and Zhang[1] previously explored the case involving equal contraction and expansion times, i.e., duty cycles of $p = 0.50$. However, they did this while also varying gaps G and actuation heights a. They observed that volumetric flow rates increased with increasing Reynolds number, beyond a *threshold* Reynolds number of 1800. That is, in their experimental setup, they only observed emergent bulk flows for $\mathrm{Re}_{in} \gtrsim 1800$. Furthermore, they saw that all volumetric flow data collapsed onto the same line when normalized by the average gap, G.

While our numerical setup was slightly different than their experimental setup, we saw similar trends in the case when $p = 0.50$ to Thiria and Zhang.[1] Figure 13 gives the (a) dimensional and (b) dimensionless net volumetric flow rates as functions of f/ν and the input Reynolds numbers, respectively, for a variety of actuation frequencies. Note that in the dimensional plot Fig. 13(a), the quantity f/ν is effectively the input Reynolds number, as neither the gap G, peak-to-peak actuation amplitude a, tooth geometry d, nor length of the pump L was varied [see Eq. (1)]. We also observed that net volumetric flow rates increase with increasing input Reynolds numbers and frequency. Similar to Ref. 1, the data collapsed to a single curve when normalized by the system's characteristic velocity, i.e., the product of frequency and actuation amplitude fa (see Sec. II). However, we observed bulk flows for much lower Re_{in} than the aforementioned threshold

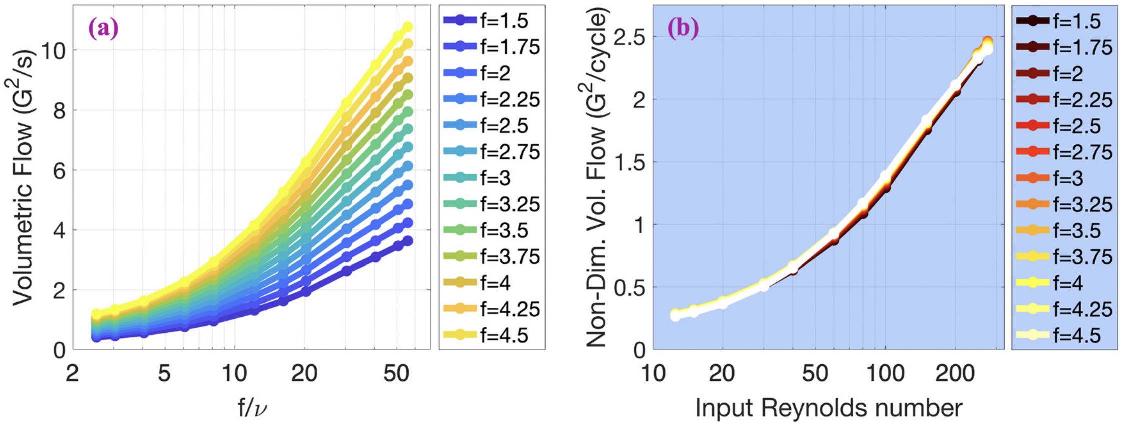

FIG. 13. Time-averaged (a) *dimensional* and (b) *non-dimensional* net volumetric flow rates corresponding to the (Re_{in}, f) subspace with duty cycle $p = 0.50$. These data were generated by the ML-gPC model.

described in Ref. 1, due to differences in our computational design. For the remainder of the manuscript, we will mainly focus on dimensionless volumetric flow rates. What has yet to be explored at this junction are any possible effects that varying duty cycles have on volumetric flow rates.

C. Effects of varying duty cycle on volumetric flow rates

We first began by exploring duty cycle effects in tandem with varying input Reynolds numbers, i.e., the (Re_{in}, p) subspace. We began by choosing three actuation frequencies $f \in \{1.25, 2.5, 3.75\}$ Hz and investigating those specific slices through the 3D parameter space. As expected, higher Re_{in} produced higher dimensionless volumetric flow rates in general, see Fig. 14. Non-linear trends emerged with variations in duty cycle beyond a critical input Reynolds number, roughly $\mathrm{Re}^*_{in} \sim 50$. More specifically, higher Re_{in} and higher duty cycle led to the largest flow rates overall. Across all three subspaces, higher Re_{in} and lower duty cycles also resulted in higher flow rates. For $\mathrm{Re}_{in} = 250$, a minimum in net dimensionless volumetric flow rate appeared across each subspace between $p \sim 0.40$ and 0.50. Further, this minimal volumetric flow rate moved toward lower duty cycles as Re_{in} decreased. While the net dimensionless volumetric flow data exhibited nonlinear behavior when varying duty cycle for $\mathrm{Re}_{in} \gtrsim \mathrm{Re}^*_{in}$, the data did not show the existence of any local maxima for $p \in (0.25, 0.75)$. This suggests that bulk transport generated by geometric asymmetry favors asymmetric actuating kinematics. The highest flow rates observed corresponded to higher duty cycles, i.e., longer contraction phases with shorter expansion phases.

Furthermore, asymmetric actuating kinematics produced differing vortex dynamics as did varying Re_{in} (see Figs. 31 and 33 in Appendix D, respectively). Given that extremal duty cycles appear to induce greater fluid transport, these two observations suggest that the formation and interaction of vortices in the teeth during a pumping cycle likely play a critical role in generating bulk flow. We will explore these dynamics more quantitatively in depth in Sec. III E.

Since we posit that vortex dynamics ultimately help mitigate net flow generation, it is unclear whether an optimal parameter subspace exists among f and p at different fluid scales. As pumping kinematics are varied, the timescales surrounding vortex formation, interaction, and dissipation are also directly affected. Therefore, we suspected that the pump exhibited nonlinear pumping performance, due to the emergence of a positive feedback loop between pump kinematics and vortex dynamics. We explored this possibility across three subspaces. Each subspace included all combinations of frequencies and duty cycles in the overall parameter space but at a specific input fluid scale: $\mathrm{Re}_{in} = 50,\ 150,$ and 250.

Figure 15 provides the net dimensionless volumetric flow across three different subspaces. Similar behavior is observed across each subspace: nonlinear trends emerged for volumetric flow rates with variations in duty cycle, and the highest duty cycles led to the highest volumetric flow rates overall. Across all subspaces, varying frequency had little effect on pump performance, i.e., volumetric flow data once again approximately collapsed to a single curve. Similar to our earlier observation from Fig. 14, a local minimum emerged in further support that higher volumetric flow rates favor asymmetric pumping kinematics. All in all, these plots suggest that variations in duty cycle elicit greater changes in time-averaged dimensionless volumetric flow rates than variations in frequency across the entire 3D target parameter space.

D. Output Reynolds number (Re_{out}) vs Strouhal number (St)

Much of the volumetric flow data can be summarized when plotting the Strouhal number (St) against an output Reynolds number (Re_{out}). Recall $\mathrm{Re}_{out} = \mathrm{Re}_{in}/\mathrm{St}$ [see Eq. (6)]. In particular, higher duty cycles (p) and input Reynolds numbers (Re_{in}) correspond to higher volumetric flow rates, whereas varying frequency did not show much of an effect. Thus, higher Re_{in} and higher p produce higher Re_{out} but lower St. Figure 16 illustrates these relationships across the 3D target parameter space. Furthermore, distinct clusters emerge in the Re_{out} $-$St space for different Re_{in} and p. On the other hand, Fig. 16(b) suggests that a given f does not guarantee where you will be in the

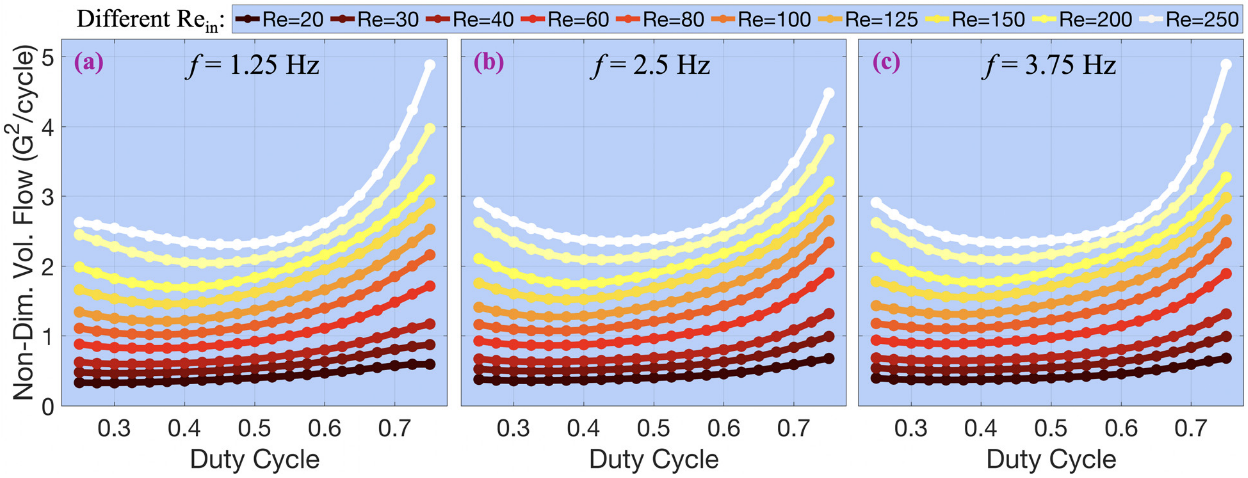

FIG. 14. Plots of time-averaged *dimensionless* net volumetric flow corresponding to three different (Re_{in}, p) subspaces, each corresponding to a different contraction frequency: (a) $f = 1.25$ Hz, (b) $f = 2.5$ Hz, and (c) $f = 3.75$ Hz. These data were generated by the ML-gPC model.

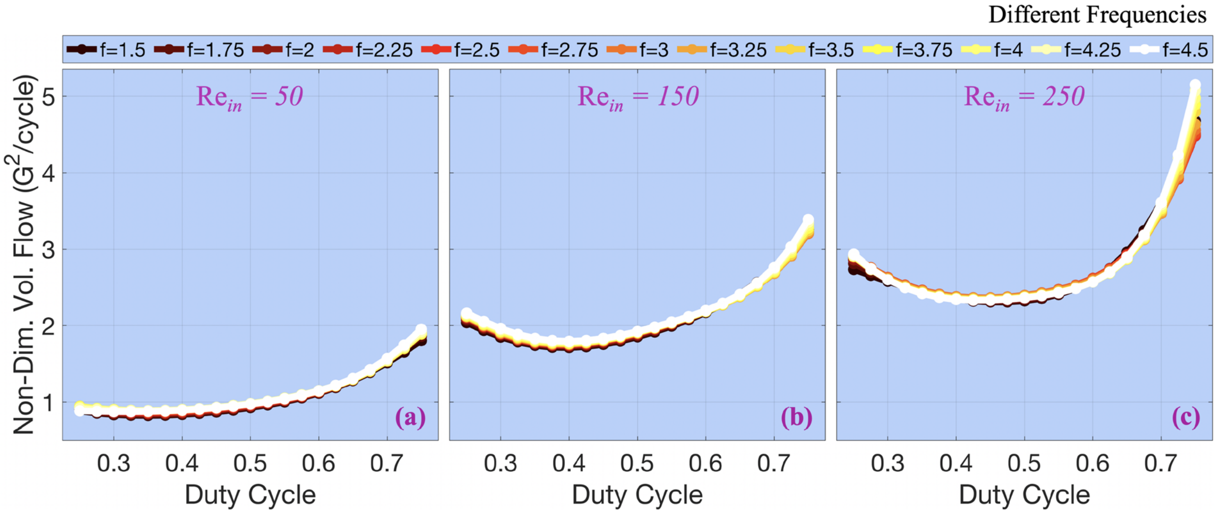

FIG. 15. Time-averaged *dimensionless* net volumetric data over slices through the subspace (f, p) corresponding to three different input Reynolds numbers: (a) $\text{Re}_{in} = 75$, (b) $\text{Re}_{in} = 150$, and (c) $\text{Re}_{in} = 250$. These data were generated by the ML-gPC model.

$\text{Re}_{out} - \text{St}$ space. Figures that deconstruct the parameter ranges from Fig. 16 are provided in Figs. 34–36 in Appendix D. As either Re_{in} or p varies, the relationship between St and Re_{out} change

$$\log \text{St} \sim -0.41 \cdot \log \text{Re}_{out} \text{ as } \text{Re}_{in} \text{ varies}$$
$$\log \text{St} \sim -1.00 \cdot \log \text{Re}_{out} \text{ as duty cycle varies.}$$

Moreover, these data can give a qualitative idea of how *sensitive* volumetric flow rates are to the three input parameters. For example, dimensionless volumetric flow rates do not appear sensitive to actuation frequency. That is, varying frequency does not substantially affect the resulting flow rate. However, varying either the input Reynolds number or duty cycle (or both) can substantially affect the resulting flow rates. These ideas are quantitatively explored further in Sec. III F.

E. Circulation analysis

Vortex dynamics are guided by geometric anisotropy and appear to be largely responsible for the pump's flow performance, as the vorticity snapshots in Figs. 10 and 12 suggest. Our hypothesis was if vortex dynamics are largely responsible for biasing bulk flow toward a preferred direction, then volumetric flow dynamics should closely follow circulation dynamics. Our general heuristic of this process was as follows: *along the bottom of the jaw, CCW vortices (positive circulation values) push bulk flow toward the left side of the pump (the outflow), while CW vortices (negative circulation) give rise to backflow toward the right end of the pump. This creates a competition between CCW and CW vortices, in that they actively work against each other's flow direction when on the other's flowward side.*

To investigate this process, we computed the fluid circulation in the bottom half of the pump, including across each tooth and halfway through the gap between the sides of the pump throughout each simulation (see Fig. 30 in Appendix D). We did this to delineate the contribution to circulation from the teeth and gap spacing. However, note that vortices that were present in the bottom half of the jaw typically extended from the gap to inside a tooth, as illustrated in Figs. 10 and 12. Therefore, much of our analysis below includes contributions to circulation from both the gap and teeth. On that note, we defined the dimensionless circulation across the gap to be $\tilde{\tilde{\Gamma}}_G$, across the teeth to

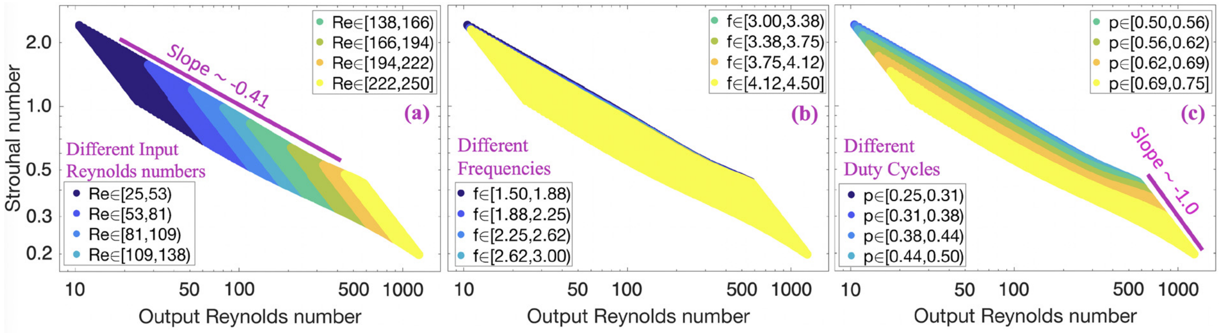

FIG. 16. Plots of the Strouhal number (St) against the output Reynolds number (Re_{out}) across the entire 3D target parameter space. Partitioning the data by different ranges of the (a) input Reynolds number, (b) pumping frequency, and (c) duty cycle. These data were generated by the ML-gPC model. See Figs. 34–36 in Appendix D for a further deconstruction of each parameter range.

be $\tilde{\tilde{\Gamma}}_T$, and across both to be $\tilde{\tilde{\Gamma}}_B$. Note that the distance halfway between both sides of the pump was dynamic; the gap $y(t)$ changed as the pump was actuated. Thus, the circulation domain was perpetually re-calculated in our analysis scripts.

Overall, we found that dimensionless net volumetric flow and $\tilde{\tilde{\Gamma}}_B$ followed the pumping kinematics, see Fig. 17. This was also consistent across different duty cycle cases. However, there were some slight discrepancies between the pumping kinematics and fluid data waveforms. For example, consider the top case, which provides data for a duty cycle case of $p = 0.30$. Although the pumping kinematics waveform was asymmetrically tilted to the right, the waveforms describing volumetric flow and $\tilde{\tilde{\Gamma}}_B$ were more heavily asymmetric but in the same direction. Nevertheless, more notable was that the net volumetric flow and $\tilde{\tilde{\Gamma}}_B$ waveforms closely resembled each other. On the other hand, for the other two duty cycle cases shown: $p = 0.55$ (middle) and $p = 0.75$ (bottom), all three waveforms closely followed one another. Figure 37 in Appendix D provides a complementary plot to Fig. 17 to further show these relationships, by non-uniformly scaling the time-dependent data across the three cases. Recall that the net volumetric flow waveforms were the result of computing the difference between the volumetric flows out of each end of the pump throughout the simulation. Thus, the observations above suggest that total circulation helped generate bulk transport in a preferred direction, thereby inducing net volumetric flows.

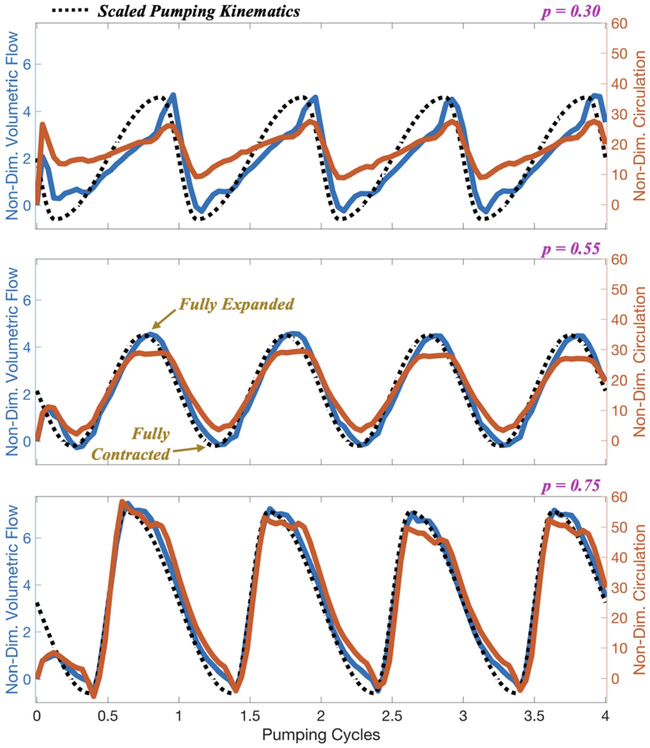

FIG. 17. Comparison of the pumping kinematics, non-dimensional net volumetric flow rates, and non-dimensional fluid circulation over time for the case when $\mathrm{Re}_{in} = 150$ involving $\nu = 0.0988\,\mathrm{cm}^2/\mathrm{s}$, $f = 3.0\,\mathrm{Hz}$, and $p = 0.30$ (top), $p = 0.55$ (middle), and $p = 0.75$ (bottom). The pumping kinematics were scaled such that the contraction and expansion phases could contrasted against the corresponding volumetric flow rates and circulation over time.

While Fig. 17 illustrated that the pumping kinematics, net volumetric flow, and circulation closely followed each other, it did not depict how circulation dynamics were affected by variations in the parameters. Such data are provided in Fig. 18. As the input Reynolds number increased, the amplitude of the $\tilde{\tilde{\Gamma}}_B$ waveform increased as well (top plot in Fig. 18). Only for smaller Re_{in} did slight changes appear in the waveform's profile. However, these observations did not appear to be the result of the vortices increasing in strength (magnitude). Figure 31 in Appendix D highlights that vorticity magnitudes did not appear to scale with Re_{in}. Rather, as Re_{in} increased, more complicated patterns of vortex formation and interaction appeared. Varying frequency alone had little effect on the $\tilde{\tilde{\Gamma}}_B$ waveform (middle plot in Fig. 18). This indicated that normalizing the circulation data by frequency also collapsed it to a single curve, similar to the volumetric flow data in previous sections. On that note, varying frequency also led to negligible differences in the circulation dynamics overall, see Fig. 32 in Appendix D for a qualitative comparison. On the other hand, variations in the duty cycle resulted in abrupt changes to circulation waveforms, including both its amplitude and shape. Snapshots of vorticity are given in Fig. 33 in Appendix D. These snapshots highlight substantial differences in the vortex dynamics overall.

All of the waveforms presented in Fig. 18 only depicted a single peak within each pumping cycle. However, circulation dynamics among all teeth along the bottom jaw ($\tilde{\tilde{\Gamma}}_T$) was much more

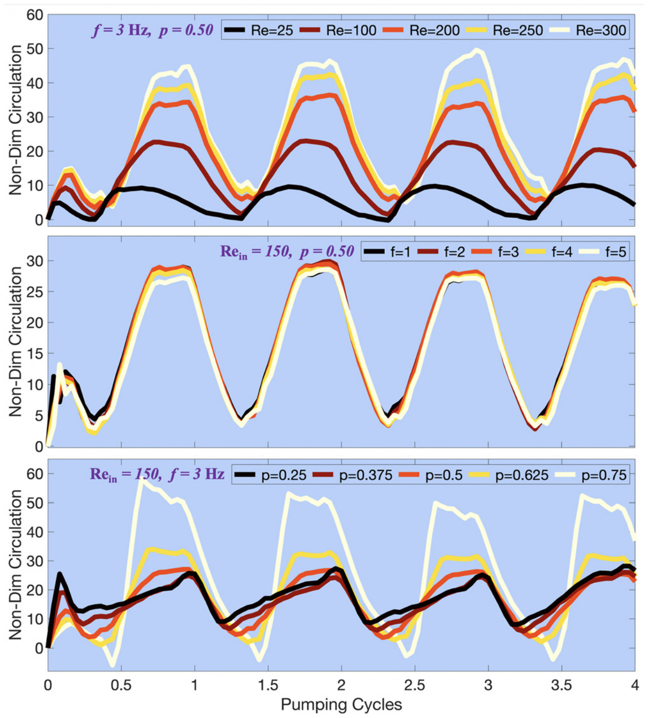

FIG. 18. Non-dimensional fluid circulation computed within the *gap and across the entire bottom jaw's teeth* $(\bar{\Gamma}_B(t))$ over the first four pumping cycles, for different perturbations of the base case involving $\mathrm{Re}_{in} = 150$ with $\nu = 0.0988\,\mathrm{cm}^2/\mathrm{s}$ and $f = 3.0\,\mathrm{Hz}$, and $p = 0.50$: (top) varying Re_{in}, (middle) varying f, and (bottom) varying p.

complicated. Multiple circulation peaks emerged in each pumping cycle, see Fig. 19. This suggested highly dynamic vortex formation and interactions occur within the teeth. Comparing Figs. 18 and 19, we noticed that the highest peaks in $\widetilde{\overline{\Gamma}}_T$ occurred at the tail end of the peaking regions in $\widetilde{\overline{\Gamma}}_B$. On the other hand, the smaller peaks in $\widetilde{\overline{\Gamma}}_T$ generally corresponded to just before $\widetilde{\overline{\Gamma}}_B$ began increasing toward its only largest peak.

While Fig. 19 presented the time evolution of circulation in the entire bottom jaw's teeth $(\widetilde{\overline{\Gamma}}_T)$, it was a metric comprising the contribution of every tooth. When looking at circulation data for each individual tooth $\widetilde{\Gamma}^k$, it was apparent that each tooth's contribution to $(\widetilde{\overline{\Gamma}}_T)$ were not equal. Circulation magnitudes were greatest for the teeth on the outer edge of the jaw, i.e., teeth 1 and 8, see Fig. 20. Recall that the teeth are labeled from right-to-left, see Fig. 1. The teeth closer to the middle had lower circulation magnitudes throughout each cycle. Moreover, these observations were consistent in all other cases analyzed, e.g., see Fig. 38 in Appendix D to see how circulation in each tooth varies for different duty cycles (for $\mathrm{Re}_{in} = 150$ with $\nu = 0.0988\,\mathrm{cm}^2/\mathrm{s}$ and $f = 3$ Hz). With this information in mind, an interesting follow-up study may be investigating the effects that different numbers of teeth have on pump performance. Similarly, knowing that the teeth nearest the edges of the jaw contributed the most to the circulation in the teeth overall, it may be interesting to explore if one could optimize the morphology of the middle teeth to further boost pumping performance rather than assume a uniform tooth morphology across the entire pump.

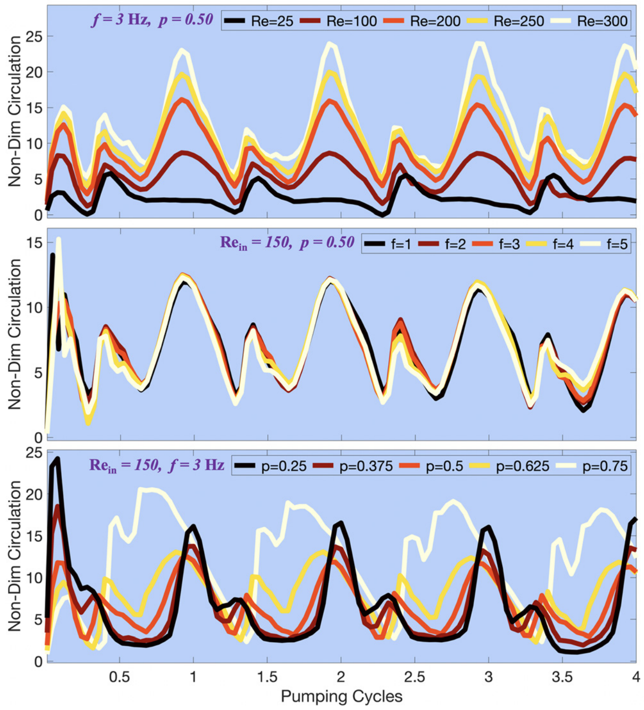

FIG. 19. Non-dimensional fluid circulation computed within the *bottom jaw's teeth only* $(\widetilde{\overline{\Gamma}}_T(t))$, over the first four pumping cycles, for different perturbations of the base case involving $\mathrm{Re}_{in} = 150$ with $\nu = 0.0988\,\mathrm{cm}^2/\mathrm{s}$ and $f = 3.0\,\mathrm{Hz}$, and $p = 0.50$: (top) varying Re_{in}, (middle) varying f, and (bottom) varying p.

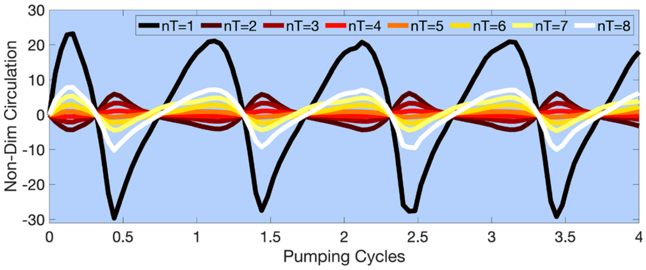

FIG. 20. Non-dimensional fluid circulation computed in each tooth along the bottom jaw in the case of $\mathrm{Re}_{in} = 150$ involving $\nu = 0.0988\,\mathrm{cm}^2/\mathrm{s}$ $f = 3.0\,\mathrm{Hz}$, and $p = 0.50$.

F. Global sensitivity analysis

Our gPC-based surrogate model allowed us to access the global sensitivity of our pump's output metrics to variations among the input parameters. That is, we were able to quantify how much of the output data's variance could be attributed to one (or more) individual parameters. We used this information to rank the relative importance of each parameter on the specific output metric. Note that although we can determine which parameter variations affect the output data the most, i.e., contribute most to the overall model output variance, this information does not tell us whether performance increased or decreased as a result of the variations. Thus, this current sensitivity analysis complements the previous performance studies from Secs. III A–III E but cannot replace them fully.

Recall that our original ML-gPC model was trained on a parameter space comprising $\mathrm{Re}_{in} \times f \times p = [1, 300] \times [1, 5] \times [0.2, 0.8]$. In this analysis, our quantities of interest included time-averaged volumetric flow and circulation ($\widetilde{\overline{\Gamma}}_B$, the combined circulation from the gap and teeth). For completeness, we also did this for both dimensional and non-dimensional quantities. Having thoroughly explored the performance of the pump over this 3D parameter space (Secs. III B–III E), we suspected that the pump's performance was most sensitive to variations

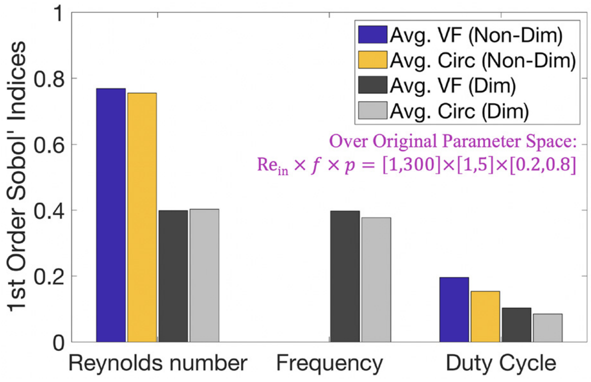

FIG. 21. First-order Sobol' sensitivity indices over the *original full parameter space*, $\mathrm{Re}_{in} \times f \times p = [1, 300] \times [1, 5] \times [0.2, 0.8]$. These indices correspond to 4 different quantities of interest: dimensional and dimensionless time-averaged volumetric flow rates and time-averaged circulation, for the three input parameters: Re_{in}, f, and p. The circulation analyzed here included contributions from both the gap and teeth, i.e., $\widetilde{\overline{\Gamma}}_B$.

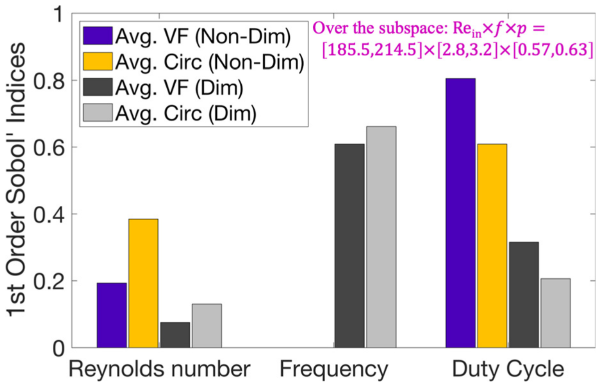

FIG. 22. First-order Sobol' sensitivity indices over a *restricted 3D parameter subspace*, $\mathrm{Re}_{in} \times f \times p = [100, 300] \times [1.25, 4.75] \times [0.225, 0.775]$. These indices correspond to four different quantities of interest: dimensional and dimensionless time-averaged volumetric flow rates and time-averaged circulation, for the three input parameters: Re_{in}, f, and p. The circulation computed here included both contributions from the gap and teeth, i.e., $\widetilde{\widetilde{\Gamma}}_B$.

TABLE II. Spatial and temporal parameters used in our FSI model.

Parameter	Variable	Units	Value
Domain Size	$[L_x, L_y]$	cm	$[13.5, 3.375]$
Spatial Grid Size	$dx = dy$	cm	$L_x/4608 = L_y/1152$
Lagrangian Grid Size	ds	cm	$dx/2$
Time Step Size	dt	s	2.5×10^{-5}
Target Stiffness	k_{target}	$\mathrm{g \cdot cm/s^2}$	1.0×10^7

in the input Reynolds number within this parameter space (e.g., see Figs. 13–16). This was formally confirmed by our Sobol' sensitivity analysis, see Fig. 21. Note that the dimensional output metrics were most sensitive to the input Reynolds number as well. This may not be too surprising since lower input Reynolds numbers always result in lower volumetric flow rates, no matter the frequency or duty cycle. Variations in frequency had negligible effects on the overall output variance among all dimensionless quantities. This agreed with our previous observations that normalizing by the frequency-based characteristic velocity (fa) resulted in the data collapsing to a single curve (e.g., Figs. 13 and 15, as well as the middle plots in Figs. 18 and 19). Moreover, the total-order Sobol' indices were similar to the first-order indices, suggesting higher-order interactions did not substantially contribute to the overall model variance, see Fig. 39 in Appendix D.

However, an interesting question remains in regard to which parameter(s) are most important if we look at a 3D parameter subspace in which there are higher volumetric flows to begin with. For example, what if we turned our attention to the original target 3D parameter space described above and focused on a smaller subspace comprising $\mathrm{Re}_{in} \times f \times p = [185.5, 214.5] \times [2.8, 3.2] \times [0.57, 0.63]$? Within this restricted 3D parameter subspace, we know that volumetric flows are high (see, for example, Figs. 13–15). Therefore, considering variations of all three parameters within this 3D subspace may substantially change the Sobol' sensitivity indices. Note that this restricted subspace can be viewed as 5% deviations away from $(\mathrm{Re}, f, p) = (200, 3, 0.6)$ given the full ranges of overall parameter

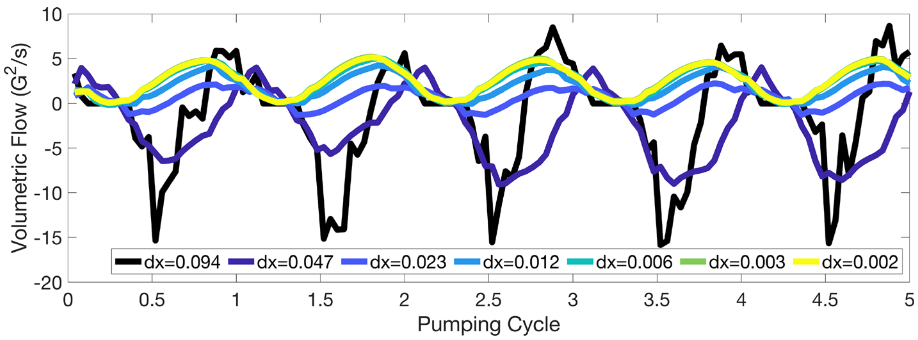

FIG. 23. Time evolution of the spatially averaged volumetric flow rate for different grid resolutions in the $\mathrm{Re}_{in} = 250$ case involving $\nu = 0.0593$, $f = 3\,\mathrm{Hz}$, and $p = 0.50$.

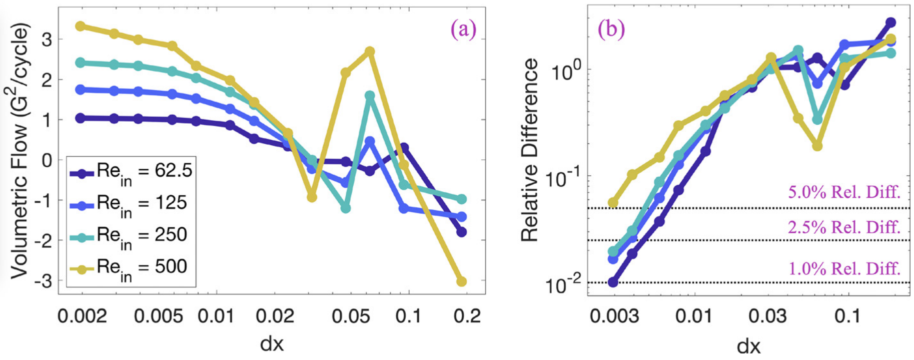

FIG. 24. (a) Spatially and time-averaged volumetric flow rates for different grid resolutions and input Reynolds numbers (Re_{in}), from parameter combinations of $\nu = 0.2371, 0.1185, 0.0593$, and 0.0296, $f = 3\,\mathrm{Hz}$, and $p = 0.50$. (b) Plot of relative differences in dimensionless volumetric flow for different Re_{in} across different grid resolutions, compared to the highest resolved case of $dx = L_x/N_x = 13.5/6912 \approx 0.002$.

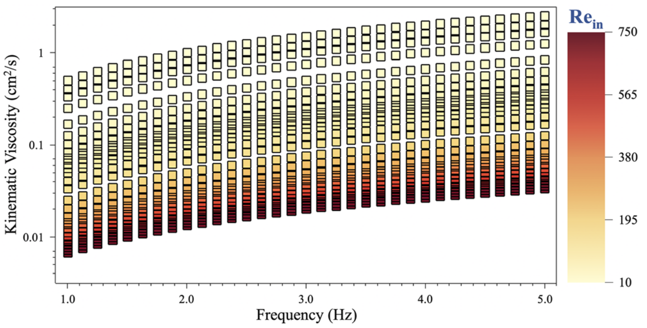

FIG. 25. Plot illustrating the relationship between the pumping frequency f and kinematic viscosity ν that provide different adjusted input Reynolds numbers, Re_{in}.

space. Furthermore, this chosen restricted subspace included a higher range of input Reynolds numbers as well as f and p ranges where our gPC model was found to be more accurate, i.e., ranges that do not include extremal values of the original parameter ranges.

Recall that the Sobol' sensitivity indices were calculated based on the gPC coefficients [see, for example, Eqs. (18) and (19)]. Fortunately, we were able to make use of the original gPC model, which was trained over the full original 3D parameter space, to train a gPC model on the 3D restricted parameter subspace. That is, we were able to bootstrap our original gPC surrogate model to construct a gPC model on the 3D subspace. Thereby, this bootstrapping procedure provided us with new gPC coefficients that correspond to a gPC trained over the restricted subspace: $\mathrm{Re}_{in} \times f \times p = [185.5, 214.5] \times [2.8, 3.2] \times [0.57, 0.63]$. This was possible since our original gPC model surrogate model was able to predict our output quantities of interest with sufficient accuracy. Thus, we could make it predict the desired output quantities of parameter combinations required for training the new bootstrapped gPC model. Note that we were able to establish accuracy in the newly acquired sensitivity indices by varying hyperparameters of the gPC, i.e., the order of the expansion, $D = \{5, 6, 7, 8, 9, 10\}$, and observing negligible differences in their resulting gPC sensitivity indices.

The sensitivity indices over the restricted 3D parameter subspace divulged a different story of parameter importance, see Fig. 22. First, the dimensionless output quantities were most affected by variations in the duty cycle in this reduced 3D subspace. On the other hand, variations in frequency most affected all dimensional output metrics. These observations were in stark contrast to when the input Reynolds number was the most important parameter, regardless of units, over

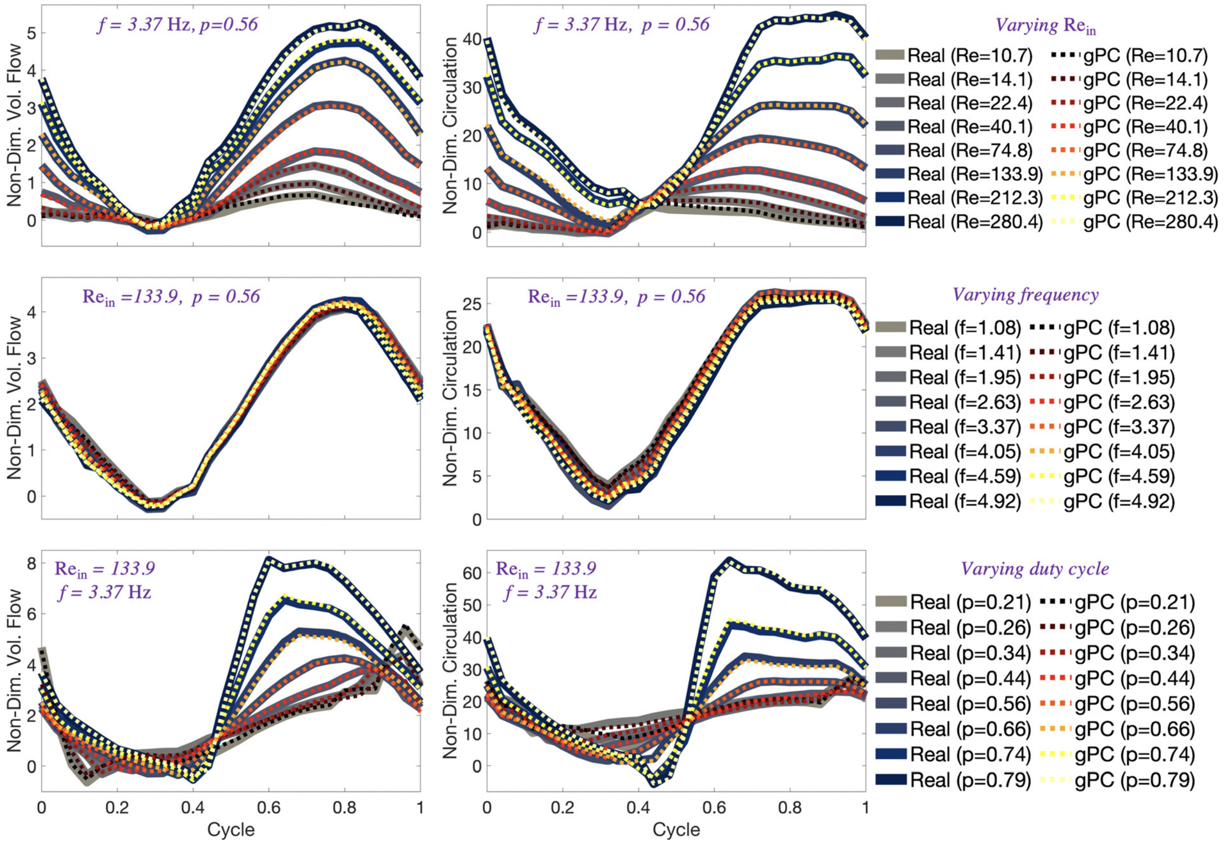

FIG. 26. Comparing the waveforms of the dimensionless (left) volumetric flow rates and (right) circulation (averaged the bottom half of the pump, both the gap and teeth, see Fig. 30) over one pumping cycle between the training data (full FSI simulations) and gPC surrogate model when (top) Re_{in} is varied, (middle row) f is varied, and (bottom row) duty cycle is varied.

the original (full) parameter space. Second, frequency minimally affected dimensionless quantities, which was consistent with the Sobol' sensitivity analysis on the full original parameter space (see Fig. 21). Third, choosing appropriate output metric units was critical to understanding the holistic performance of the pump. That is, here the duty cycle was deemed the most important parameter for dimensionless quantities in a subspace that exhibited high pumping performance. Such dimensionless quantities were defined and normalized by the pumping frequency. However, dimensional metrics were most sensitive to variations in pumping frequency. Therefore, if trying to optimize a physical model, it is critical to decide how you will be measuring your output, i.e., in what units, to understand the variance observed due to different design parameters. Finally, once again, the total-order Sobol' indices were similar to the first-order indices, suggesting that higher-order interactions did not contribute much to the overall variance in the output in the restricted parameter subspace, see Fig. 40 in Appendix D.

IV. DISCUSSION AND CONCLUSIONS

In this work, we demonstrated how geometric anisotropy can induce bulk fluid flow in a preferred direction. More specifically, we showed that volumetric flow rates are driven by fluid vorticity (circulation) within the pump itself. We also identified how pumping kinematics (frequency and duty cycle) affect pump performance, along with scale (an input Reynolds number). Higher input Reynolds numbers and higher duty cycles produced higher dimensionless volumetric flow rates. Variations in frequency were negligible for dimensionless volumetric flow, which agreed with the scaling observations of Thiria and Zhang.[1] Moreover, this was later formally confirmed in our global sensitivity analysis, where frequency was the least important parameter for the pump's dimensionless quantities of interest. Performance metrics were most sensitive to the input Reynolds number on the full parameter space: $\mathrm{Re}_{in} \times f \times p = [1, 300] \times [1, 5] \times [0.2, 0.8]$. On the other hand, in a reduced 3D parameter subspace ($\mathrm{Re}_{in} \times f \times p = [185.5, 214.5] \times [2.8, 3.2] \times [0.57, 0.63]$), we observed that duty cycle became the most important parameter for dimensionless output metrics, while frequency remained nearly negligible. Interestingly, this substantially changed for dimensional metrics; they were most sensitive to frequency.

Much of this study was only possible by taking a machine learning (ML) approach using generalized polynomial chaos expansions (gPC). Once trained, validated, and tested, gPC alleviated the necessity for performing computationally expensive fluid-structure interaction simulations. Not only were we able to accurately predict time-averaged performance metrics, but we were able to use our ML-gPC approach to predict time-series data corresponding to our metrics, as well, e.g., volumetric flow rates and circulation over time. We remark that gPC accuracy slightly decreased when predicting output metrics near the edges of the parameter space on which it was trained. This likely was an artifact of the sampling approach used to collect training data (see Sec. II B). Overall, this framework allowed us to quickly and accurately predict performance outputs on any lower-dimensional subspaces of the full 3D target space. Furthermore, gPC allowed us to assess the

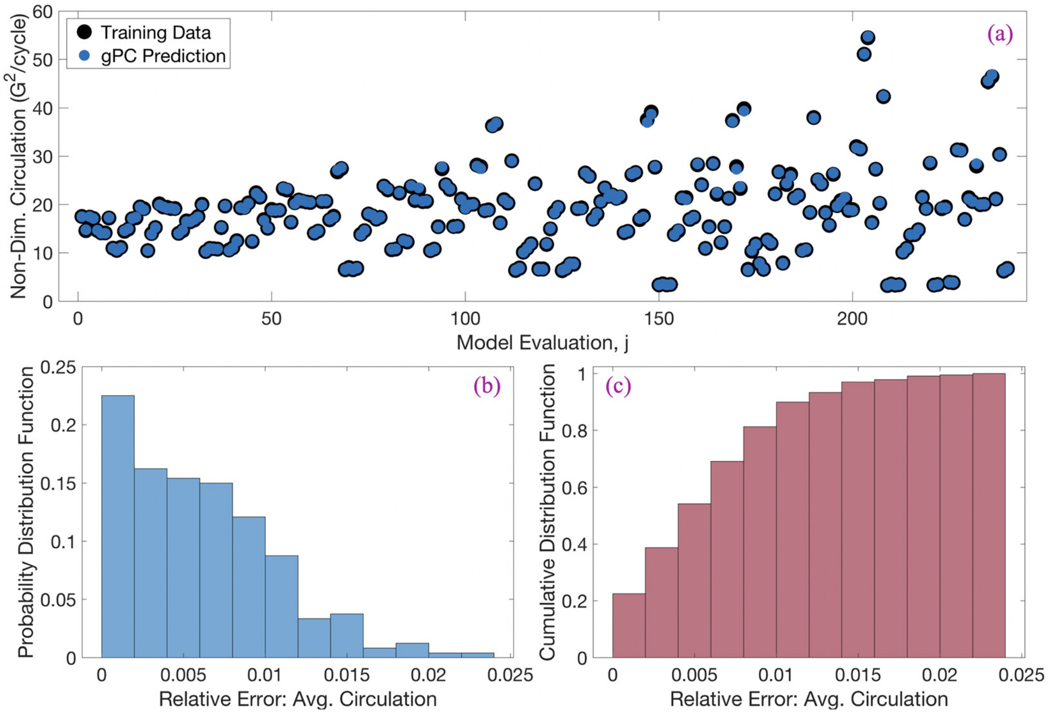

FIG. 27. (a) Qualitative comparison between the full FSI simulated training dataset involving dimensionless circulation (in the bottom half of the pump, both the gap and teeth, see Fig. 30) and the gPC-surrogate's predicted values. (b) Probability distribution function and (c) cumulative distribution function of the relative errors from those data in (a). Figure 6 in Sec. II C provides a similar figure but for dimensionless volumetric flow rates.

global sensitivity of our model's outputs over variations in a 3D parameter space. To that extent, since gPC is a surrogate framework, we could bootstrap it to perform sensitivity analysis on a restricted proper 3D subspace of the original 3D space that the gPC was trained over.

Although this study focused on understanding how variations in three parameters (an adjusted input Re, frequency, and duty cycle) affected pump performance, there are many other interesting avenues to pursue in light of these results. For example, in this work the actuation amplitude was held constant; however, previous valveless pumping studies have shown the relative importance of compression ratio on bulk flow rates.[15,66–69] Also, as briefly mentioned in Sec. III E, from having learned that the outer teeth along the pump most contribute to intertooth circulation $(\overline{\Gamma}_T)$, this begs the question of how many teeth are necessary in the pump to reap the performance benefits of geometric anisotropy. This was also posited by Chrispell *et al.*[19] Furthermore, in tandem, one could also vary the relative positions of the teeth on the top and bottom of the pump to one another. Here, we assumed symmetry across the gap, although one may be inclined to relax this notion. Finally, one could also try modulating the shape of the interior teeth to harness circulation in an effort to optimize bulk transport. Since cavity morphology, i.e., the teeth in this work has been shown to heavily influence vortex formation, topology, and dynamics,[70–72] it may be possible to design an overall anisotropic geometry that optimizes volumetric flow via fluid ratcheting.

Previous efforts by Chrispell *et al.*[19] observed interesting behavior when ratcheting viscoelastic fluids using a similar geometry. Nonlinear behavior emerged when varying Weissenberg number (We), that is, the degree of viscoelasticity. Their data suggested that there is an optimal We before volumetric fluxes become impeded. Thus, combining similar efforts of this study and the ideas proposed above but with a pump immersed in a viscoelastic fluid may lead to unsuspected nonlinear behavior.

However, attempting to holistically study these proposed perturbations in concert would be computationally challenging using the ML-gPC method implored in this work. As the dimension of target design parameter space increases, the amount of training data, i.e., independent fluid-structure simulations, required to train the gPC increases substantially. For example, using the same empirical rules and polynomial degrees as this work (see Sec. II), if one wanted to explore a 4, 5, or 6-dimensional parameter space, it would require 990, 3168, or 8580 independent FSI simulations, respectively. Note that

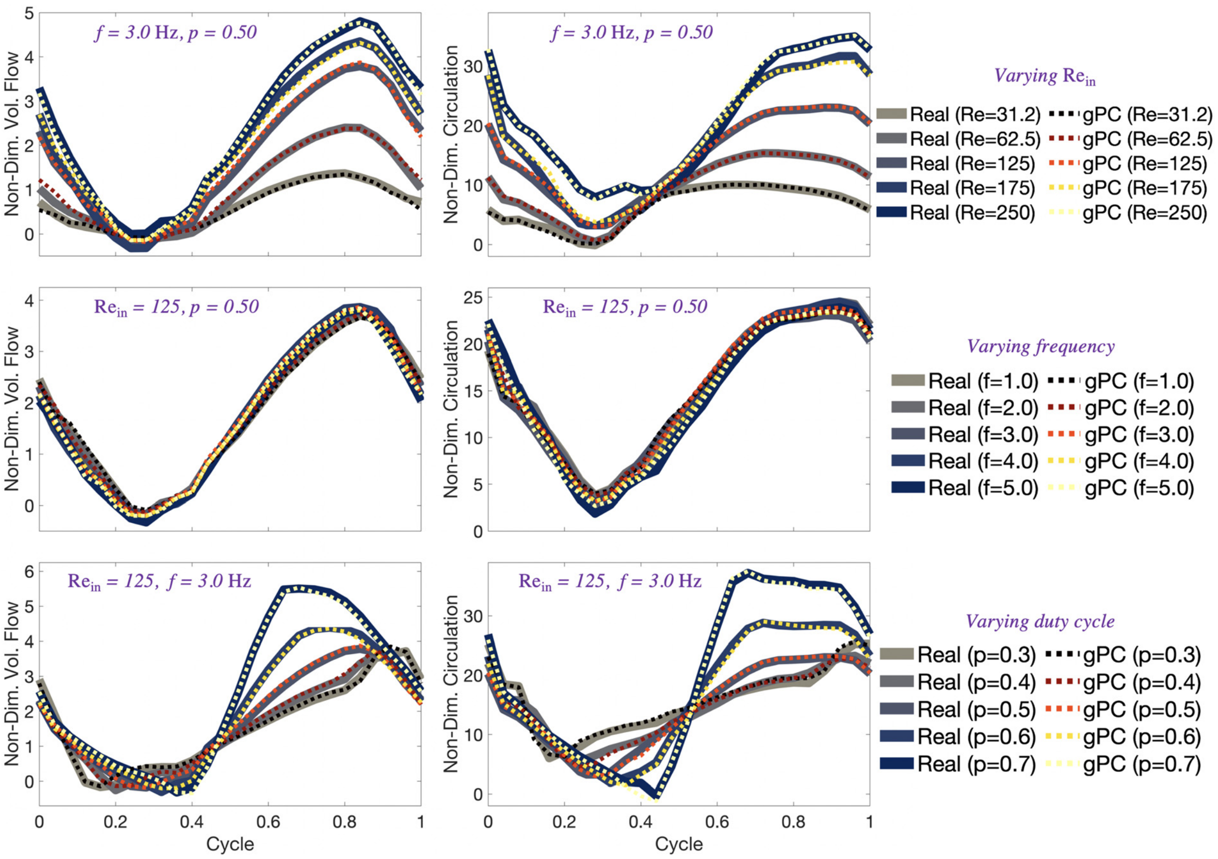

FIG. 28. Comparing the waveforms of the dimensionless (left) volumetric flow rates and (right) circulation (averaged the bottom half of the pump, both the gap and teeth, see Fig. 30) over one pumping cycle between the test data (full FSI simulations) and gPC surrogate model when (top) Re$_{in}$ is varied, (middle row) f is varied, and (bottom row) duty cycle is varied.

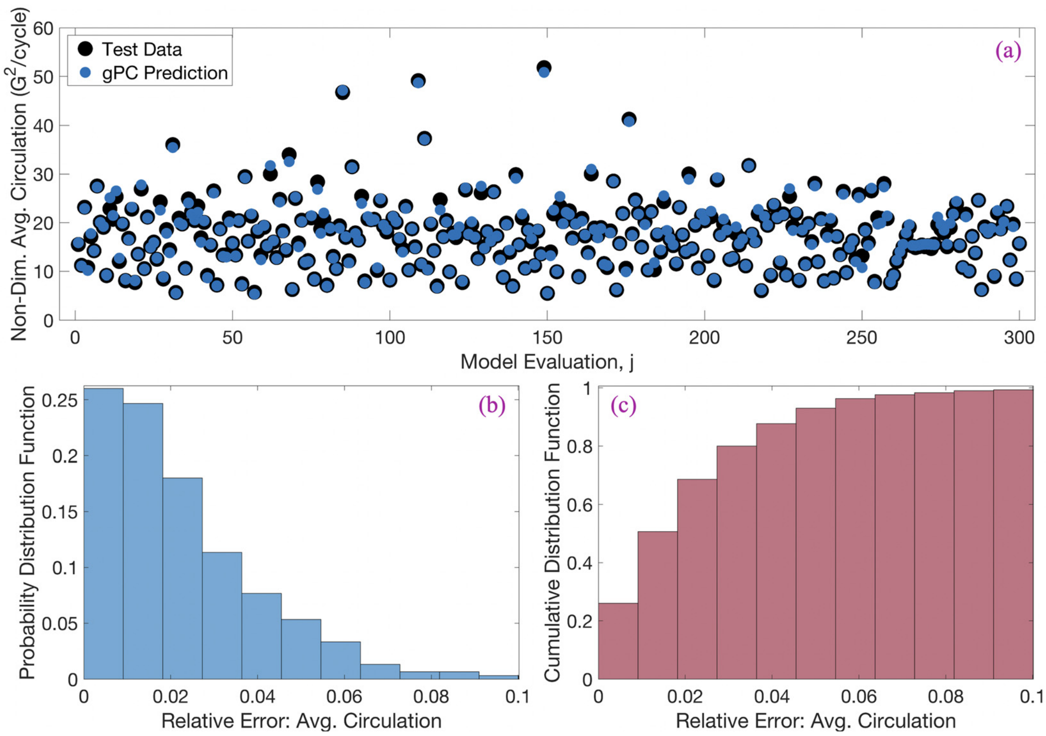

FIG. 29. (a) Qualitative comparison between the full FSI simulated test dataset involving dimensionless circulation (in the bottom half of the pump, both the gap and teeth, see Fig. 30) and the gPC-surrogate's predicted values. (b) Probability distribution function and (c) cumulative distribution function of the relative errors from those data in (a). Figure 8 in Sec. II D provides a similar figure but for dimensionless volumetric flow rates.

these estimates are solely for training the gPC and do not include the number of independent simulations required for testing the gPC's accuracy. Thus, the curse of dimensionality still rears its ugly head. Moreover, ML-gPC has the restriction that its 'hyper-parameters' are selected *a prior*. That is, one first selects the polynomial degree which determines how the training points are sampled (see Sec. II B). There are a variety of other surrogate model frameworks.[73] One popular framework is feedforward neural networks (FNNs),[74–76] which are well known to be universal function approximators.[77] FNNs offer the flexibility of hyperparameter selection once all data have been collected; however, there is ambiguity when it comes to optimal sampling strategies and the amount of training data to collect.

If design optimization is only of interest, an alternative method could be using the method of *active subspaces*. Active subspace assesses gradients of a model's output to construct a response surface in a lower dimensional space.[78,79] It has been successfully applied to numerous problems, including optimizing the design of an aircraft wing within a 50-dimensional parameter space. The low-dimensional subspaces it found revealed global trends within the overall 50-dimensional space.[80] Despite its successes, traditionally active subspaces have suffered from two drawbacks. First, an inability to know *a priori* how many model evaluations (simulations) must be performed, beyond *ad hoc* estimates.[81] Since FSI model evaluations are computationally expensive, performing sequential model evaluations once gradients are uncovered, after successive rounds of parameter space sampling, could be impractical. Second, improper sampling of the parameter space could lead to sub-optimal solutions.[81] However, numerous research efforts have focused on alleviating these ailments.[81–85] Either way, such an active subspace framework may forgo one's ability to holistically interpret the pump's performance across the entire high dimensional parameter

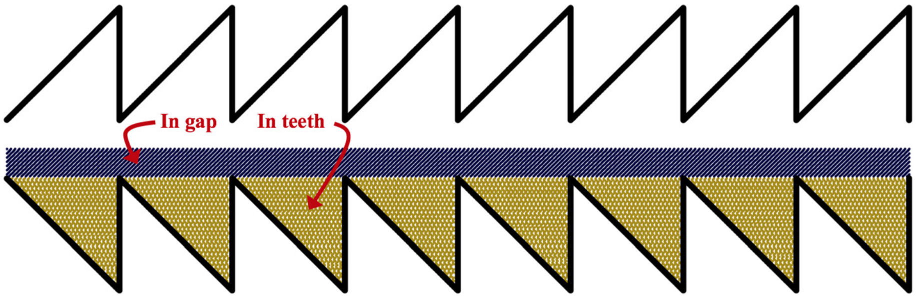

FIG. 30. Depicting the regions in which circulation was computed through each simulation.

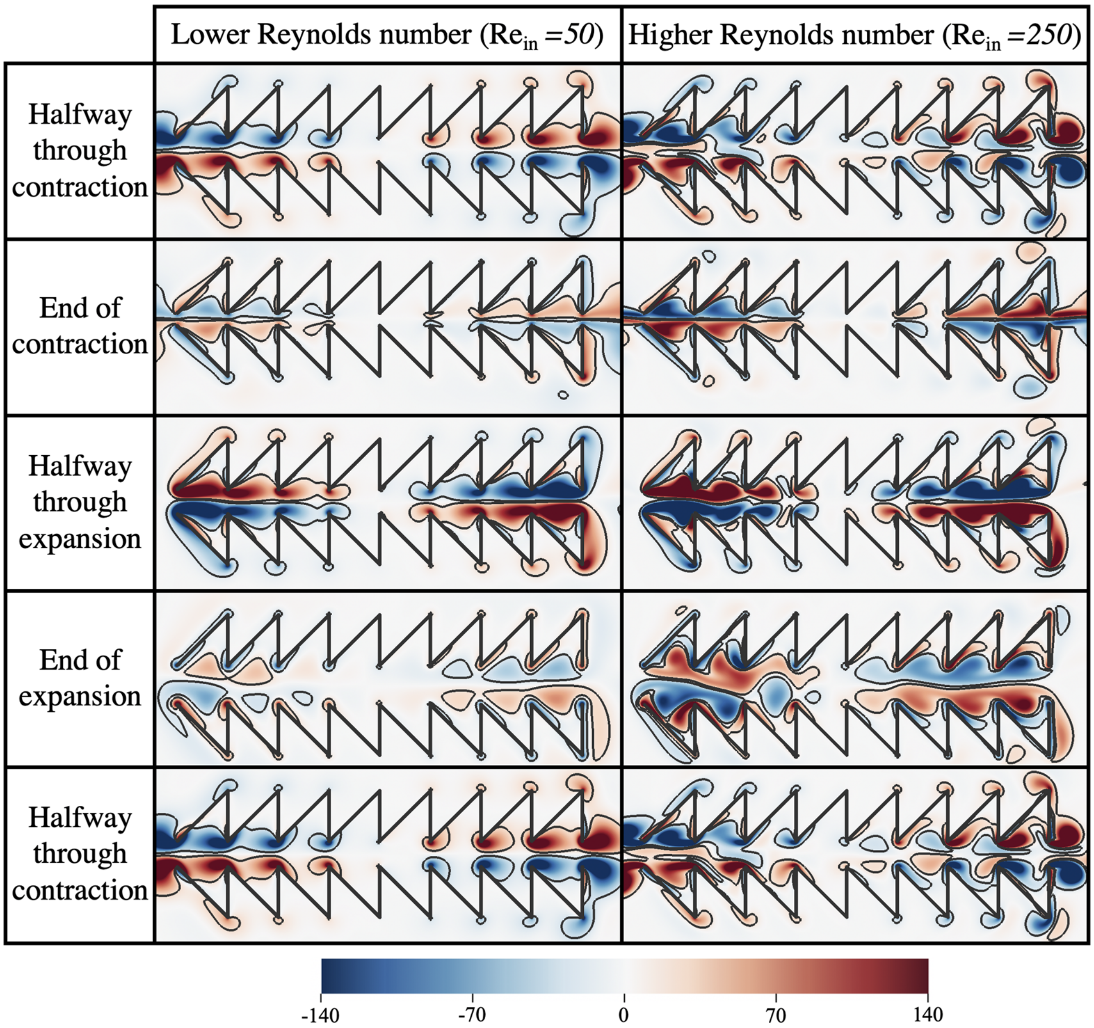

FIG. 31. Colormaps illustrating snapshots of vorticity (with vorticity contours) for cases involving input Reynolds numbers of $Re_{in} = 50$ (left) and 250 (right) when frequency and duty cycle are fixed at 3.0 Hz and 0.50, using $\nu = 0.2963$ and $0.0593\,cm^2/s$, respectively. Note that the time points depicted are from the start of the second to third pumping cycle and that the colormaps are identical between both cases.

space. Although global sensitivity can be assessed using active subspaces,[86] one benefit of the ML-gPC approach here is that we were able to construct a surrogate model to predict performance over the entire parameter space. Once trained, the gPC could also be bootstrapped to explore global sensitivity within any subspace of the full overall parameter space; this could be computationally challenging using active subspaces, without performing more expensive FSI simulations.

ACKNOWLEDGMENTS

The authors would also like to thank Christina Battista, Matthew Mizuhara, Mary Salcedo, Emily Slesinger, and Christopher Strickland for their comments and discussion. Computational resources and support were provided by the NSF OAC (Grant Nos. 1826915, 1828163, and 2320244). Support for ZM was provided by TCNJ's Mentored Undergraduate Summer Experience (MUSE) Program. Support for NAB was provided by the TCNJ Support of Scholarly Activity (SOSA) Grant, TCNJ Sabbatical Program, and NSF DMS (Grant No. 2410987). Support for L.A.M. was provided by NSF (Grant No. 2152110).

AUTHOR DECLARATIONS

Conflict of Interest

The authors have no conflicts to disclose.

Author Contributions

Zain Moin: Conceptualization (equal); Data curation (equal); Formal analysis (equal); Visualization (equal); Writing – original draft (equal); Writing – review & editing (equal). **Laura A. Miller:** Conceptualization (equal); Writing – original draft (equal); Writing – review & editing (equal). **Nicholas A. Battista:** Conceptualization

(equal); Data curation (equal); Formal analysis (equal); Funding acquisition (equal); Investigation (lead); Methodology (lead); Project administration (lead); Resources (equal); Software (lead); Supervision (lead); Validation (lead); Visualization (equal); Writing – original draft (lead); Writing – review & editing (lead).

DATA AVAILABILITY

The data that support the findings of this study are available from the corresponding author upon reasonable request.

APPENDIX A: DETAILS REGARDING THE IMMERSED BOUNDARY METHOD (IB)

Here, the *immersed boundary method* (IB)[87] will be briefly introduced. The IB is a fluid-structure interaction method that solves the equations that couple the motion of an immersed structure to the fluid in which it is immersed. The open-source IB software IB2d[41–43] was used for all the simulations presented in this work.

The full viscous, incompressible Navier–Stokes equations were used to model the fluid system at the intermediate Reynolds numbers considered, i.e.,

$$\rho\left[\frac{\partial \mathbf{u}}{\partial t}(\mathbf{x},t) + (\mathbf{u}(\mathbf{x},t)\cdot\nabla)\mathbf{u}(\mathbf{x},t)\right] = -\nabla p(\mathbf{x},t) + \mu\Delta\mathbf{u}(\mathbf{x},t) + \mathbf{f}(\mathbf{x},t), \quad \text{(A1)}$$

$$\nabla\cdot\mathbf{u}(\mathbf{x},t) = 0, \quad \text{(A2)}$$

where $\mathbf{u}(\mathbf{x},t)$ and $p(\mathbf{x},t)$ are the fluid's velocity and pressure, respectively, at spatial location $\mathbf{x}$ at time t. $\mathbf{f}(\mathbf{x},t)$ is the force per unit area applied to the fluid by the immersed boundary, i.e., the

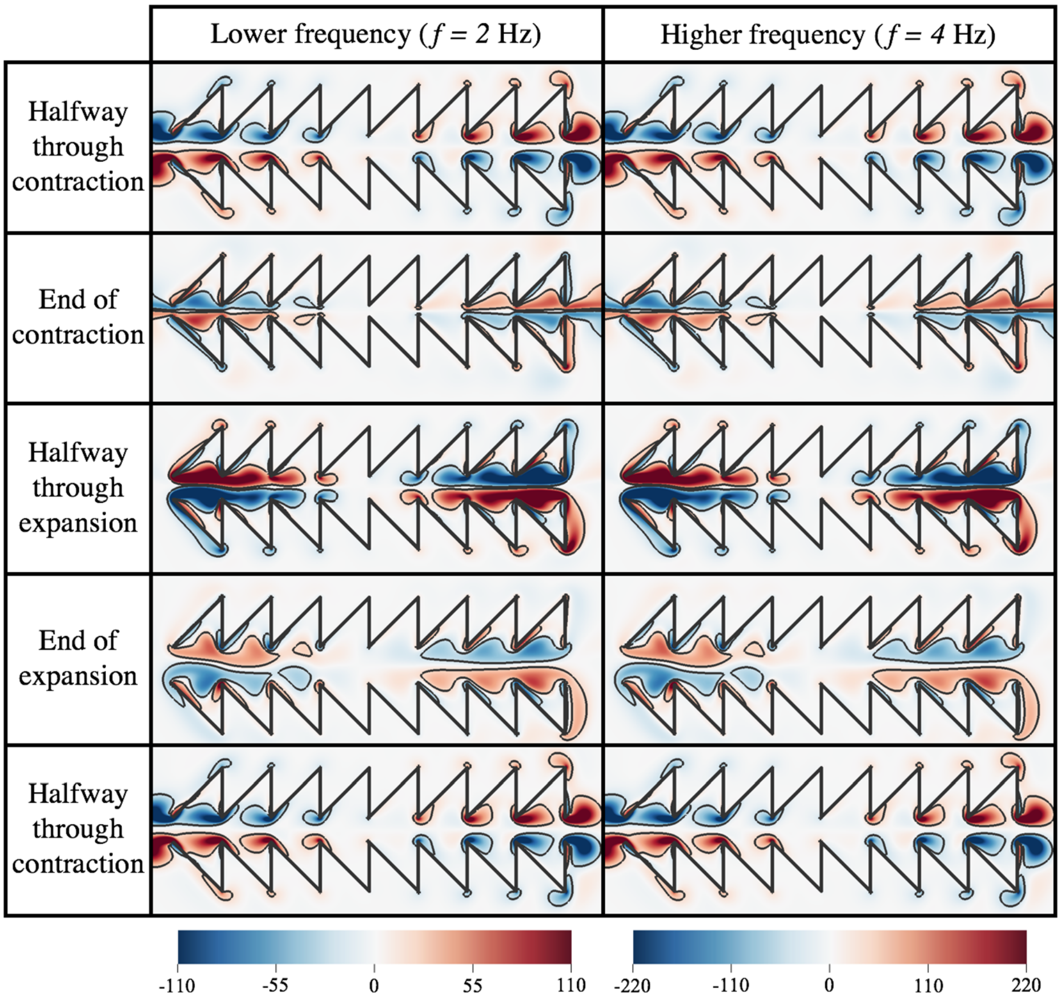

FIG. 32. Colormaps illustrating snapshots of vorticity (with vorticity contours) for cases involving $f = 2.0$ Hz (left) and $f = 4.0$ Hz (right) when the input Reynolds number and duty cycle are fixed at 150 (using $\nu = 0.0658$ and $0.1317\ \mathrm{cm}^2/\mathrm{s}$) and $p = 0.50$, respectively. Note that the time points depicted are from the start of the second to third pumping cycle and that the colormaps are identical between both cases.

ratcheting pump. These three quantities are modeled in an Eulerian framework on a fixed rectangular mesh. ρ and μ are the fluid's density and dynamic viscosity, respectively.

All *interactions* between the pump and fluid are governed by integral equations with delta function kernels, see Eqs. (A3) and (A4). While the pumping motion is prescribed, the fluid's behavior is not. As the pump oscillates, forces are spread from it onto the nearest fluid mesh points, which in turn push the fluid to move. On the other hand, while the fluid's velocity is interpolated back onto the pump to ensure the no-slip condition is satisfied, it has little effect on the pump. This is due to the pump's rigidity and prescribed pumping dynamics [see Eq. (A5)]; the pump resists non-prescribed motion. The integral equations that govern these dynamics are given as

$$\mathbf{f}(\mathbf{x},t) = \int \mathbf{F}(s,t)\delta(\mathbf{x}-\mathbf{X}(s,t))ds, \tag{A3}$$

$$\frac{\partial \mathbf{X}}{\partial t}(s,t) = \int \mathbf{u}(\mathbf{x},t)\delta(\mathbf{x}-\mathbf{X}(s,t))d\mathbf{x}. \tag{A4}$$

$\mathbf{X}(s,t)$ and $\mathbf{F}(s,t)$ give the Cartesian coordinates and deformation forces along the immersed boundary (the pump) for each point denoted by Lagrangian parameter s and at time t, respectively. Equations (A3) and (A4) essentially transform Lagrangian variables to Eulerian variables and vice versa. Here, $\delta(\mathbf{x})$ is a 2D delta function. These delta functions help to ensure that forces from the immersed body are spread only to the nearest fluid mesh points to the immersed boundary and vice versa, when the velocity field is interpolated back to the immersed boundary.

To create the pump's sawtooth geometry, each Lagrangian point was chosen to be a distance half the grid's resolution away from its neighbors, i.e., $ds = 0.5dx$ where ds and dx are the distances between successive Lagrangian points and the grid resolution,

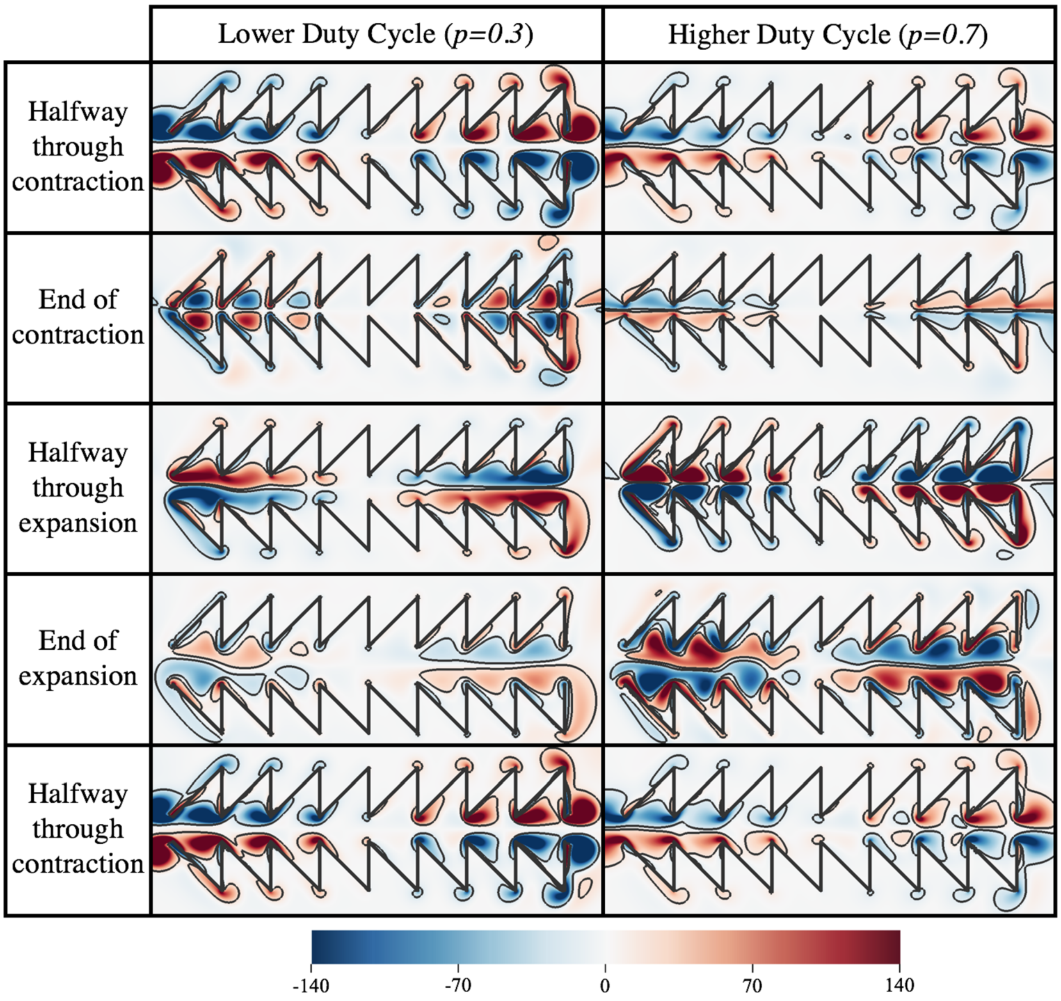

FIG. 33. Colormaps illustrating snapshots of vorticity (with vorticity contours) for cases involving $p = 0.30$ (left) and 0.70 (right) when the input Reynolds number and frequency are fixed at 150 and 3.0 Hz, respectively, using $\nu = 0.0988\,\text{cm}^2/\text{s}$. Note that the time points depicted are from the start of the second to third pumping cycle and that the colormaps are identical between both cases.

respectively. Once the pump's sawtooth geometry was constructed, each Lagrangian point was tethered to a *target point*, via a virtual spring. The pump's upper jaw's actuation was performed by dynamically updating the preferred position of each target point along the entire sawtooth geometry [see Eq. (2)]. The bottom jaw was held nearly rigid by enforcing static target point positions. Both of these actions were possible by applying a force proportional to the distance between the location of the actual Lagrangian point and its preferred target position, i.e., the target point force formulation, see Eq. (A5). Using a large value of k_{target} helps to mitigate only minor deviations between the actual position and its preferred position. The governing deformation force equation is given as follows:

$$\mathbf{F}_{target} = k_{target}(\mathbf{Y}_A(t) - \mathbf{X}_A(t)), \tag{A5}$$

where k_{target} is the stiffness coefficient and $\mathbf{X}_A(t)$ and $\mathbf{Y}_A(t)$ are the actual position of the Lagrangian point and the prescribed position of its target point, respectively. Table II provides all of the spatial and temporal discretization parameters used in our study.

To discretize (A3) and (A4) regularized delta functions from Ref. 87 were used, i.e., $\delta_h(\mathbf{x})$

$$\delta_h(\mathbf{x}) = \frac{1}{h^2}\phi\left(\frac{x}{h}\right)\phi\left(\frac{y}{h}\right), \tag{A6}$$

where $\phi(r)$ is defined as

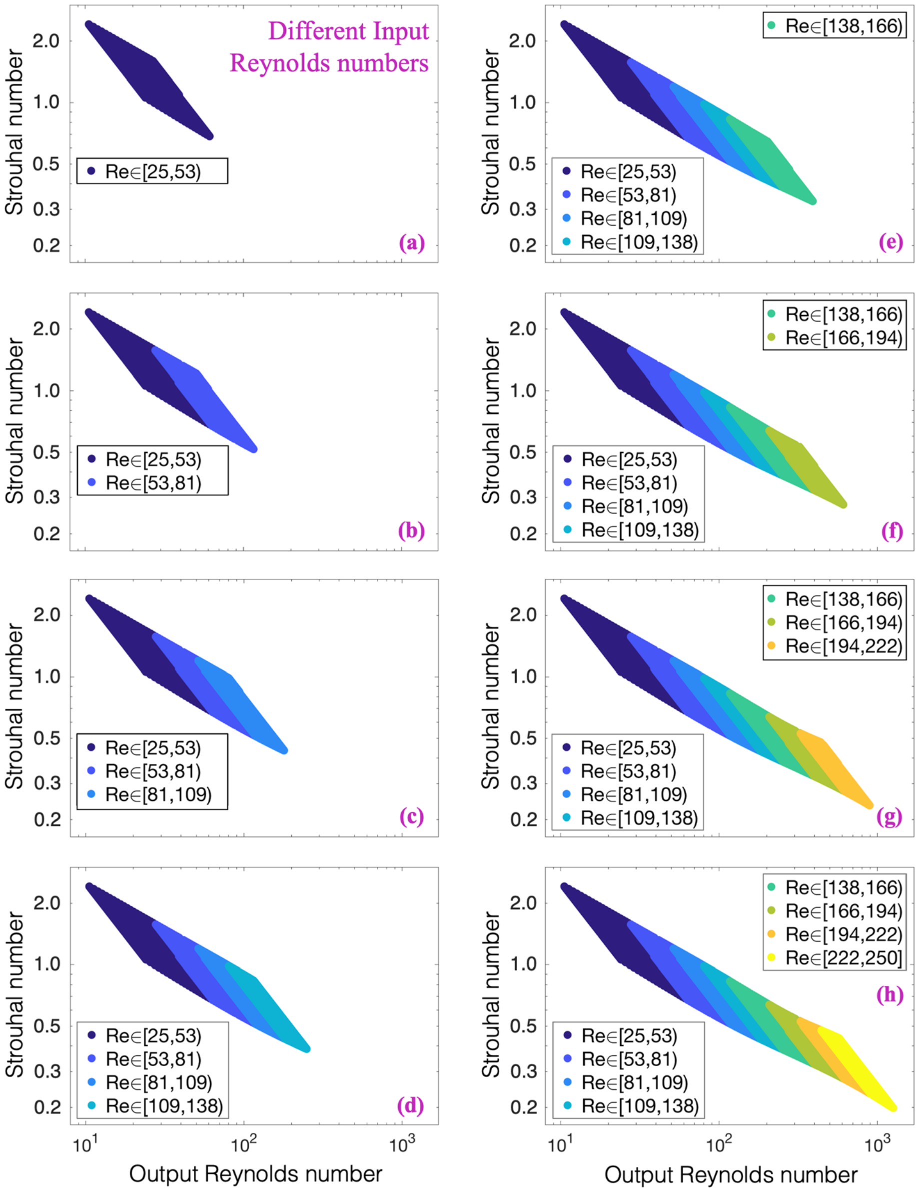

FIG. 34. Deconstructing Fig. 16(a) to show the breadth to which each range of input Reynolds number spans in the space of Strouhal number vs output Reynolds number. Each subfigure introduces a new range of input Reynolds number (Re_{in}): (a) [25,53), (b) [53,81), (c) [81,109), (d) [109,138), (e) [138,166), (f) [166,194), (g) [194,222), and (h) [222,250].

$$\phi(r) = \begin{cases} \frac{1}{8}\left(3 - 2|r| + \sqrt{1 + 4|r| - 4r^2}\right), & 0 \le |r| < 1, \\ \frac{1}{8}\left(5 - 2|r| + \sqrt{-7 + 12|r| - 4r^2}\right), & 1 \le |r| < 2, \\ 0, & 2 \le |r|. \end{cases} \tag{A7}$$

APPENDIX B: CONVERGENCE STUDY OF THE FSI MODEL

We performed convergence tests with respect to volumetric flow rates across seven different grid resolutions $dx = L_x/N_x$, where $L_x = 13.5$ and $N_x = 144$, 288, 576, 1152, 2304, 4608, and 6912. Figure 23 provides the time evolution of spatially averaged volumetric flow for a $\mathrm{Re}_{in} = 250$ case comprising $\nu = 0.059\,\mathrm{cm}^2/\mathrm{s}, f = 3\,\mathrm{Hz}$, and $p = 0.50$. The case when $dx = L_x/4608$ looks qualitatively similar to the case when $dx = L_x/6912$. Figure 24(a) provides the spatially and time-averaged dimensionless volumetric flow rate for a variety of grid resolutions as well as Reynolds numbers, $\mathrm{Re}_{in} = 62.5$, 125, 250, and 500, all with the same frequency and duty cycle, $f = 3\,\mathrm{Hz}$ and $p = 0.5$, but viscosities of $\nu = 0.2371$, 0.1185, 0.0593, and 0.0296, respectively.

Figure 24(b) provides the relative difference for the average dimensionless volumetric flow rate between the highest resolved

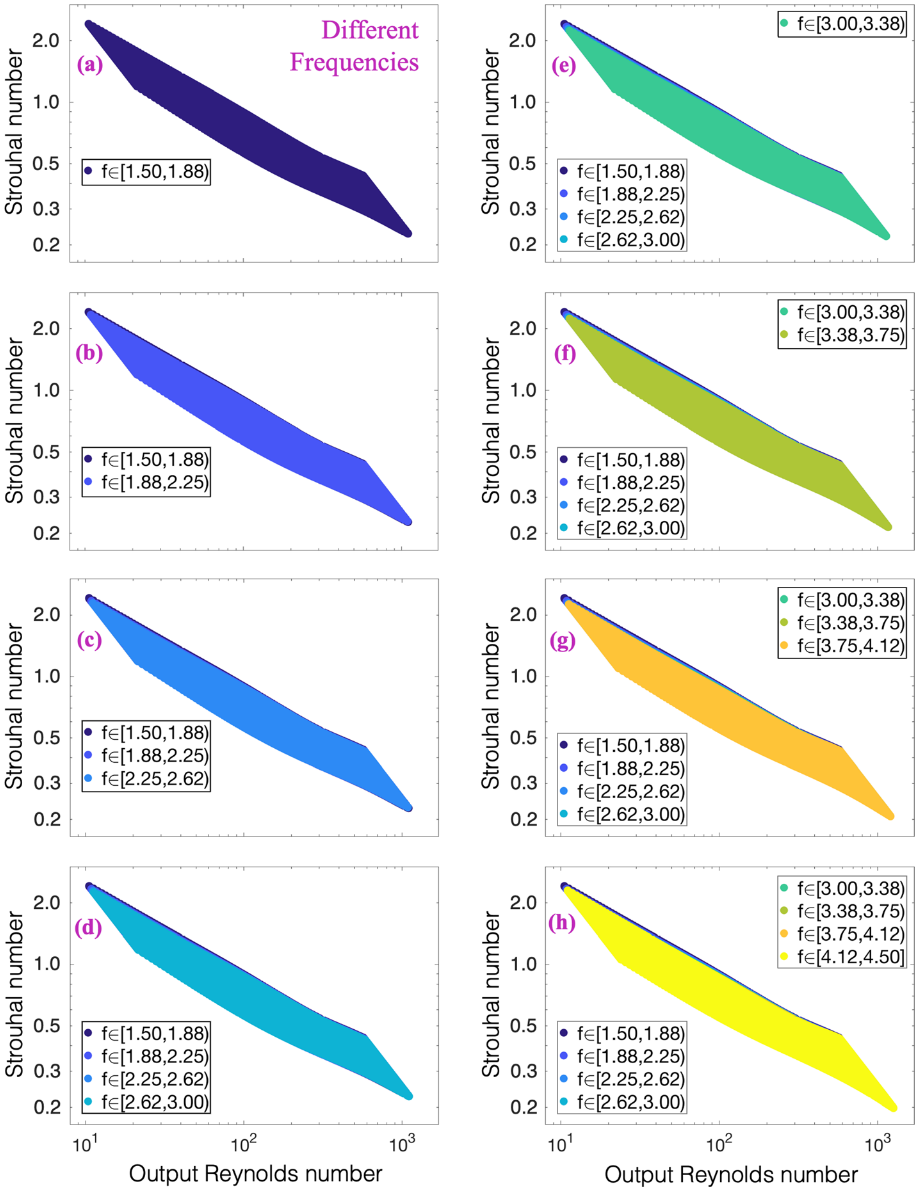

FIG. 35. Deconstructing Fig. 16(b) to show the breadth to which each range of frequency values spans in the space of Strouhal number vs output Reynolds number. Each subfigure introduces a new range of frequency (f): (a) [1.5,1.88), (b) [1.88,2.25), (c) [2.25,2.62), (d) [2.62,3.0), (e) [3.0,3.38), (f) [3.38,3.75), (g) [3.75,4.12), and (h) [4.12,4.5].

grid resolution case of $N_x = 6912$ and all other grid resolutions tested. The relative differences when considering the $N_x = 4608$ discretization are 1.00%, 1.66%, and 1.96% for Reynolds numbers of 62.5, 125, and 250, respectively. The case when $\mathrm{Re}_{in} = 500$ resulted in a relative error of 5.63%. In the remainder of the study, we used a grid discretization of $N_x = 4608$ for the sake of computational cost (both time and storage) and its relative agreement with the more refined grid of $N_x = 6912$. Moreover, to try to minimize numerical errors, we elected to only consider model evaluations with $\mathrm{Re} \lesssim 300$. Thus, we restricted our study to $\mathrm{Re}_{in} < 300$. Note that to generate the training dataset for the gPC model, the highest Re_{in} value simulated was 280.41, from combinations of $(f, \nu) = (1.949, 0.0343), (2.633, 0.0464), (3.367, 0.0593)$, and $(4.051, 0.0713)$.

APPENDIX C: GPC STATISTICS

Given a gPC expansion in the form

$$S(\vec{\xi}) = \sum_{j=0}^{\mathcal{P}-1} c_j \Psi(\vec{\xi}),$$

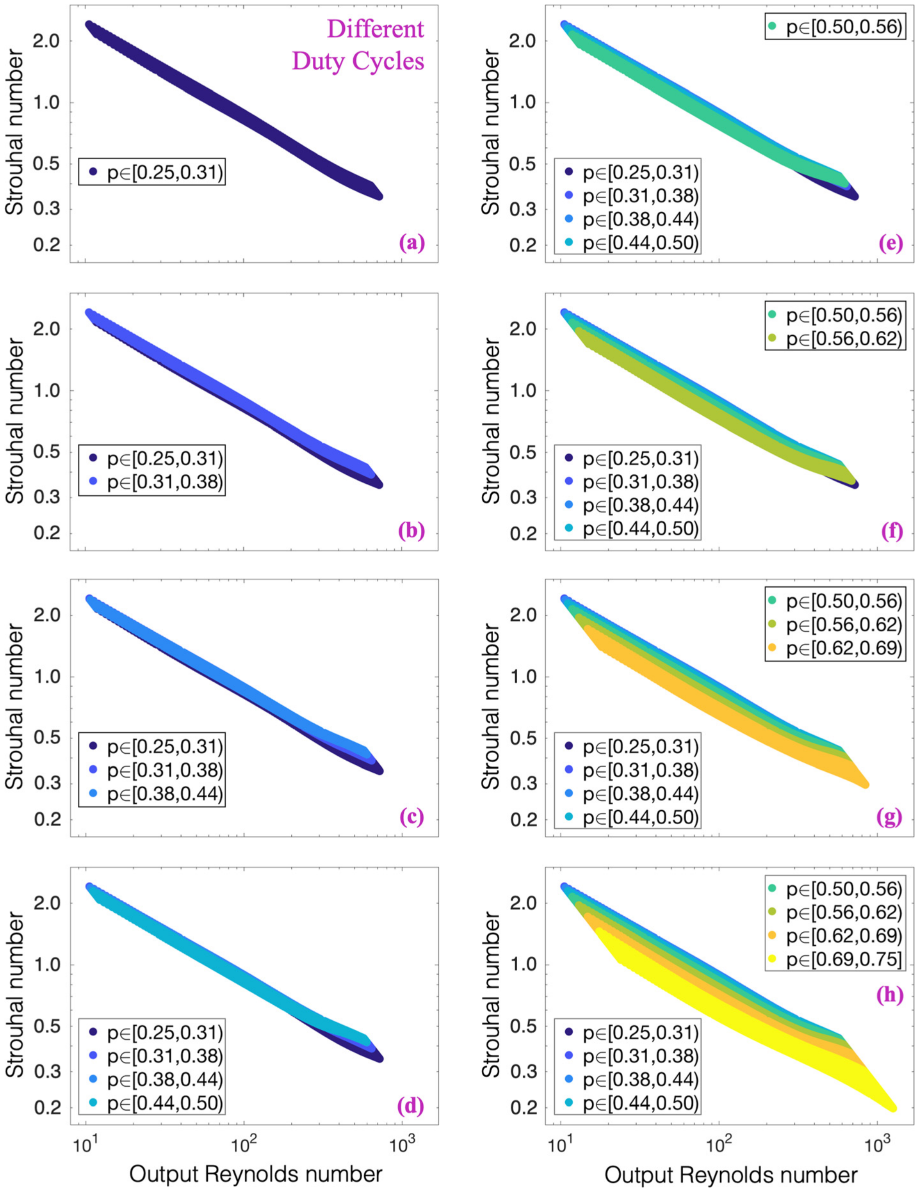

FIG. 36. Deconstructing Fig. 16(c) to show the breadth to which each range of duty cycle values spans in the space of Strouhal number vs output Reynolds number. Each subfigure introduces a new range of duty cycle (p): (a) [0.25,0.31), (b) [0.31,0.38), (c) [0.38,0.44), (d) [0.44,0.50), (e) [0.50,0.56), (f) [0.56,0.62), (g) [0.62,0.69), and (h) [0.69,0.75].

with ξ_i each scaled to be within $[-1.1]$, we can derive the expansion's mean and variance from the coefficients $\{c_j\}_{j=0}^{\mathcal{P}-1}$ and properties of multivariate Legendre polynomials. Note that $\Psi_0(\vec{\xi}) = 1$.

The derivation for the mean is as follows:

$$\begin{aligned}
\bar{S} &= E[S] = \int_\Omega S \cdot \phi(x)\, d\Omega = \int_\Omega \sum_{j=0}^{\mathcal{P}-1} c_j \Psi_j(\vec{\xi}) \cdot 1\, d\Omega \\
&= \sum_{j=0}^{\mathcal{P}-1} c_j \int_\Omega \Psi_j(\vec{\xi}) \cdot 1\, d\Omega = \sum_{j=0}^{\mathcal{P}-1} c_j \cdot E\left[\Psi_j(\vec{\xi}) \cdot 1\right] \\
&= \sum_{j=0}^{\mathcal{P}-1} c_j \cdot E\left[\Psi_j(\vec{\xi}) \cdot \Psi_0(\vec{\xi})\right] = \sum_{j=0}^{\mathcal{P}-1} c_j \cdot \frac{1}{2(j)+1}\delta_{j0} \\
\bar{S} &= c_0 \cdot \frac{1}{2(0)+1} = c_0.
\end{aligned}$$

Thus, the mean of a particular output is given by the first coefficient c_0, which is the coefficient of the $\Psi_0 = 1$ multidimensional Legendre polynomial [see Eq. (11)].

The derivation for the overall model variance for a specific output metric that the gPC was trained on is given as follows:

$$\begin{aligned}
D &= \mathrm{Var}[S] = E\left[(S-c_0)^2\right] = \int_\Omega \left(\sum_{j=0}^{\mathcal{P}-1} c_j \Psi_j(\vec{\xi}) - c_0\right)^2 d\Omega \\
&= \int_\Omega \left(\sum_{j=0}^{\mathcal{P}-1} c_j \Psi_j(\vec{\xi})\right)^2 - 2 \cdot c_0 \cdot \sum_{j=0}^{\mathcal{P}-1} c_j \Psi_j(\vec{\xi}) + c_0^2\, d\Omega \\
&= \int_\Omega \sum_{j=0}^{\mathcal{P}-1} c_j^2 \Psi_j^2(\vec{\xi})\, d\Omega - 2\int_\Omega c_0 \Psi_0(\vec{\xi}) \cdot c_j \Psi_j(\vec{\xi})\, d\Omega + \int_\Omega c_0^2 \Psi_0(\vec{\xi})^2\, d\Omega \\
&= \int_\Omega \sum_{j=1} c_j^2 \Psi_j^2\, d\Omega + \int_\Omega c_0^2 \Psi_0^2\, d\Omega - 2\int_\Omega c_0^2 \Psi_0^2\, d\Omega + \int_\Omega c_0^2 \Psi_0^2\, d\Omega \\
&= \sum_{j=1} c_j^2 \int_\Omega \Psi_j^2(\vec{\xi})\, d\Omega
\end{aligned}$$

$$D = \sum_{j=1} c_j^2 \cdot E\left[\Psi_j^2\right].$$

Note that for the multidimensional Legendre polynomials

$$E\left[\Psi_j^2\right] = E\left[\Psi_j(\xi_1, \xi_2, \ldots, \xi_M)^2\right] = \prod_{n=1}^{M} \frac{1}{2(\ell_n)+1},$$

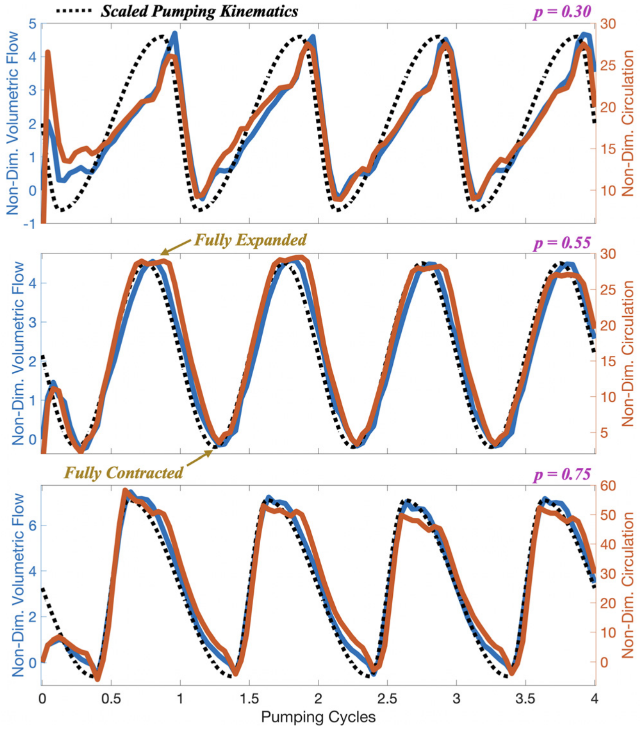

FIG. 37. Comparison of the pumping kinematics, non-dimensional net volumetric flow rates, and non-dimensional fluid circulation over time for the case when $Re_{in} = 150$ involving $\nu = 0.0988\,\mathrm{cm}^2/\mathrm{s}$, $f = 3.0\,\mathrm{Hz}$, and $p = 0.30$ (top), $p = 0.55$ (middle), and $p = 0.75$ (bottom). The pumping kinematics were scaled such that the contraction and expansion phases could contrasted against the corresponding volumetric flow rates and circulation over time. This figure complements Fig. 17. In this figure, the data were non-uniformly scaled across the three cases to highlight that the volumetric flow rates and circulation waveforms closely resemble one another.

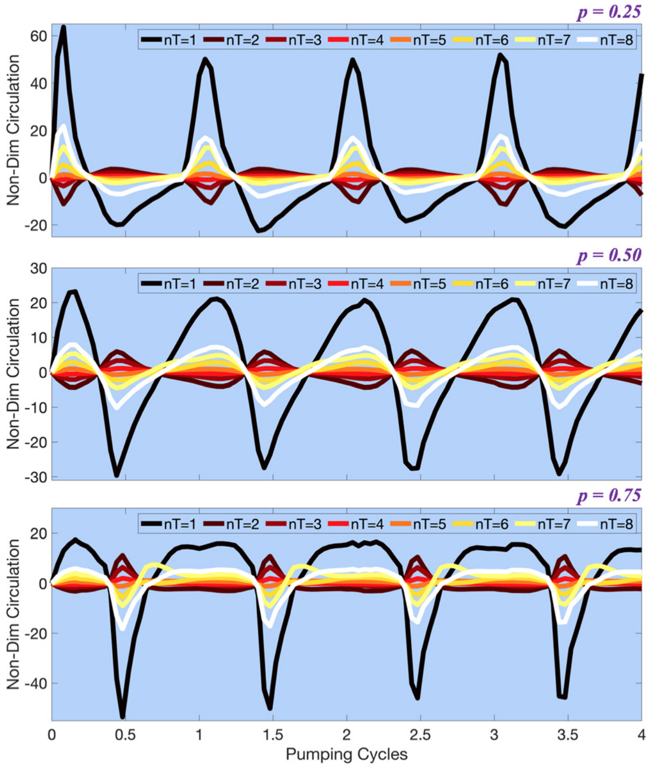

FIG. 38. Non-dimensional fluid circulation computed in each tooth along the bottom jaw in the case of $Re_{in} = 150$ and $f = 3.0\,\mathrm{Hz}$ using $\nu = 0.0988\,\mathrm{cm}^2/\mathrm{s}$, for (top) $p = 0.25$, (middle) 0.50, and (bottom) 0.75.

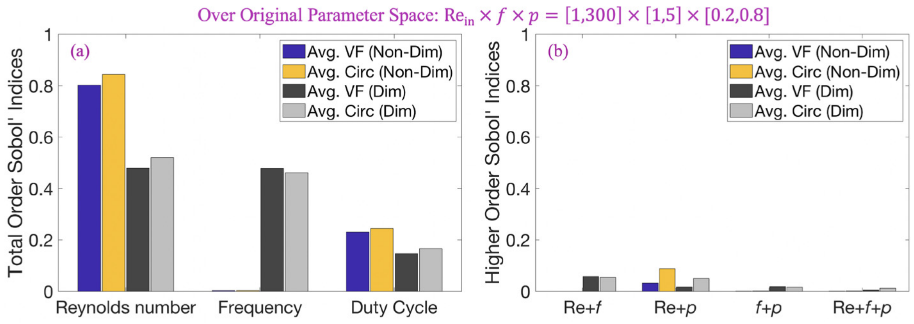

FIG. 39. (a) Total-order and (b) higher-order Sobol' sensitivity indices over the *original full parameter space*, $\mathrm{Re}_{in} \times f \times p = [1, 300] \times [1, 5] \times [0.2, 0.8]$. These indices correspond to four different quantities of interest: dimensional and dimensionless time-averaged volumetric flow rates and time-averaged circulation, for the three input parameters: Re_{in}, f, and p. The circulation computed here included both contributions from the gap and teeth, i.e., $\widetilde{\overline{\Gamma}}_B$.

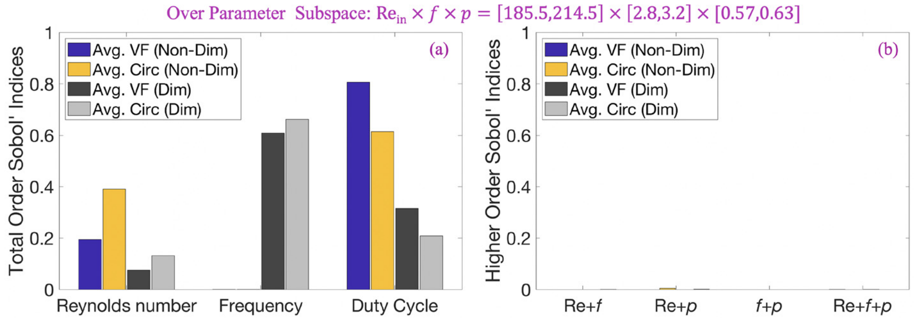

FIG. 40. (a) Total-order and (b) higher-order Sobol' sensitivity indices over a *restricted 3D parameter subspace*, $\mathrm{Re}_{in} \times f \times p = [100, 300] \times [1.25, 4.75] \times [0.225, 0.775]$. These indices correspond to four different quantities of interest: dimensional and dimensionless time-averaged volumetric flow rates and time-averaged circulation, for the three input parameters: Re_{in}, f, and p. The circulation computed here included both contributions from the gap and teeth, i.e., $\widetilde{\overline{\Gamma}}_B$.

where ℓ_n is the specific order of the nth one-dimensional Legendre polynomial that comprises the jth multi-dimensional Legendre polynomial Ψ_j, i.e.,

$$\Psi_j(\xi_1, \xi_2, \ldots, \xi_M)^2 = \prod_{n=1}^{M} \mathcal{L}_n^{\ell_n}(\xi_n).$$

See Sec. II B for more details.

APPENDIX D: ADDITIONAL FIGURES

The relationship between the desired pumping frequency f, kinematic viscosity ν, and the adjusted input Reynolds number Re_{in} is provided in Fig. 25.

REFERENCES

[1] B. Thiria and J. Zhang, "Ratcheting fluid with geometric anisotropy," Appl. Phys. Lett. **106**, 054106 (2015).

[2] S. Vogel, *Cats' Paws and Catapults* (W. W. Norton and Company, New York, NY, 1998).

[3] H. Liu, S. Ravi, D. Kolomenskiy, and H. Tanaka, "Biomechanics and biomimetics in insect-inspired flight systems," Philos. Trans. R Soc. London B Biol. Sci. **371**, 20150390 (2016).

[4] R. Salazar, V. Fuentes, and A. Abdelkefi, "Classification of biological and bioinspired aquatic systems: A review," Ocean Eng. **148**, 75–114 (2018).

[5] F. Robicsek, "Leonardo da Vinci and the sinuses of Valsalva," Ann. Thoracic Surg. **52**, 328–335 (1991).

[6] K. Keele and C. Pedretti, *Leonardo Da Vinci, Corpus of the Anatomical Studies*, Collection of Her Majesty the Queen at Windsor Castle Vol. 2 (Johnson Reprint Company, 1978).

[7] C. Peskin, "Flow patterns around heart valves: A numerical method," J. Comput. Phys. **10**(2), 252–271 (1972).

[8] A. A. V. Steenhoven and M. E. H. van Dongen, "Model studies of the closing behaviour of the aortic valve," J. Fluid Mech. **90**, 21–36 (1979).

[9] C. S. Peskin, "Numerical analysis of blood flow in the heart," J. Comput. Phys. **25**, 220–252 (1977).

[10] B. J. Bellhouse, F. Bellhouse, J. A. Abbott, and L. Talbot, "Mechanism of valvular incompetence in aortic sinus dilatation," Cardiovasc. Res. **7**, 490–494 (1973).

[11] D. Rinderknecht and M. Gharib, "A bioinspired pump for space applications," Acta Futura **6**, 9–16 (2013).

[12] Z. Li *et al.*, "Biohybrid valveless pump-bot powered by engineered skeletal muscle," Proc. Natl. Acad. Sci. U. S. A. **116**, 1543–1548 (2019).

[13] R. Davtyan and N. A. Sarvazyan, "Output of a valveless Liebau pump with biologically relevant vessel properties and compression frequencies," Sci. Rep. **11**, 11505 (2021).

[14] A. S. Forouhar *et al.*, "The embryonic vertebrate heart tube is a dynamic suction pump," Science **312**, 751–753 (2006).

[15] A. Baird, T. King, and L. A. Miller, "Numerical study of scaling effects in peristalsis and dynamic suction pumping," in *Biological fluid dynamics: modeling, computations, and applications* (AMS, 2014), Vol. 628, pp. 129–148, see https://www.ams.org/books/conm/628/conm628-endmatter.pdf

[16] N. A. Battista, A. N. Lane, and L. A. Miller, "On the dynamic suction pumping of blood cells in tubular hearts," in *Women in Mathematical Biology: Research Collaboration*, edited by A. Layton and L. A. Miller (Springer, New York, NY, 2017), Chap. 11, pp. 211–231.

[17] J. Yu, "Fluid ratcheting by oscillating channel walls with sawteeth," J. Fluid Mech. **761**, 305–328 (2014).

[18] P. Westerbaan, "Computational analysis of a fluid ratchet for pumping of Newtonian and viscoelastic fluids," Ph.D. thesis (Indiana University of Pennslyvania, 2016).

[19] J. Chrispell, E. Jenkins, and P. Westerbaan, "Simulation of ratcheting non-Newtonian fluids using a geometric anisotropy," Math. Comput. Simul. **188**, 436–454 (2021).

[20] L. Hamers, "Industrial pump inspired by flapping bird wings: New ratcheting pump uses vibrations instead of traditional rotor to transport fluids" (2015), https://www.aip.org/publishing/journal-highlights/industrial-pump-inspired-flapping-bird-wings (accessed 01 February 2023).

[21] J. F. Hillyer and G. Pass, "The insect circulatory system: Structure, function, and evolution," Annu. Rev. Entomol. **65**, 121–143 (2020).

[22] C. Blatter, E. F. J. Meijer, T. P. Padera, and B. J. Vakoc, "Simultaneous measurements of lymphatic vessel contraction, flow and valve dynamics in multiple

lymphangions using optical coherence tomography," J. Biophotonics **11**, e201700017 (2018).

[23] B. E. Flammang and M. E. Porter, "Bioinspiration: Applying mechanical design to experimental biology," Integr. Comp. Biol. **51**, 128–132 (2011).

[24] S. N. Patek, "Biomimetics and evolution," Science **345**, 1448–1449 (2014).

[25] D. Xiu and G. E. Karniadakis, "The Wiener–Askey polynomial chaos for stochastic differential equations," SIAM J. Sci. Comput. **24**, 619–644 (2002).

[26] D. Xiu, D. Lucor, C. H. Su, and G. E. Karniadakis, "Performance evaluation of generalized polynomial chaos," in *Proceedings of the International Conference on Computational Science*, edited by P. Sloot (Springer, Berlin, Heidelberg, Germany, 2003), Chap. 36, pp. 346–354.

[27] J. D. Jakeman, M. Perego, and W. M. Severa, "Neural networks as surrogates of nonlinear high-dimensional parameter-to-prediction maps," Tech. Rep. SAND2018-11042, LDRD Project No. 212725, Sandia National Laboratories, 2018.

[28] I. M. Sobol, "Global sensitivity indices for nonlinear mathematical models and their Monte Carlo estimates," Math. Comput. Simul. **55**, 271–280 (2001).

[29] B. Sudret, "Global sensitivity analysis using polynomial chaos expansions," Rel. Eng. Syst. Safety **93**(7), 964–979 (2008).

[30] X. Wei, H. Chang, B. Feng, and Z. Liu, "Sensitivity analysis based on polynomial chaos expansions and its application in ship uncertainty-based design optimization," Math. Problems Eng. **2019**, 7498526.

[31] E. Torre, S. Marelli, P. Embrechts, and B. Sudret, "Data-driven polynomial chaos expansions for machine learning regressions," J. Comp. Phys. **388**, 601–623 (2019).

[32] G. Shahzadi and A. Soulaïmani, "Deep neural network and polynomial chaos expansion-based surrogate models for sensitivity and uncertainty propagation: An application to a rockfill dam," Water **13**, 1830 (2021).

[33] A. Saltelli, "Making best use of model evaluations to compute sensitivity indices," Comp. Phys. Commun. **145**, 280–297 (2002).

[34] K. G. Link *et al.*, "A local and global sensitivity analysis of a mathematical model of coagulation and platelet deposition under flow," PLoS One **13**(7), e0200917 (2018).

[35] A. Saltelli *et al.*, "Why so many published sensitivity analyses are false: A systematic review of sensitivity analysis practices," Environ. Model. Software **114**, 29–39 (2019).

[36] I. M. Sobol, "Distribution of points in a cube and approximate evaluation of integrals," USSR Comput. Maths. Math. Phys. **7**, 86–112 (1967).

[37] D. Xiu and G. E. Karniadakis, "Modeling uncertainty in flow simulations via generalized polynomial chaos," J. Comp. Phys. **187**, 137–167 (2003).

[38] T. Göpel and C. S. Wirkner, "Morphological description, character conceptualization and the reconstruction of ancestral states exemplified by the evolution of arthropod hearts," PLoS One **13**, e0201702 (2018).

[39] T. Kodama, Y. Hatakeyama, S. Kato, and S. Mori, "Visualization of fluid drainage pathways in lymphatic vessels and lymph nodes using a mouse model to test a lymphatic drug delivery system," Biomed. Opt. Express **6**, 124–134 (2015).

[40] S. Schulte-Merker, A. Sabine, and T. V. Petrova, "Lymphatic vascular morphogenesis in development, physiology, and disease," J. Cell Biol. **193**, 607–618 (2011).

[41] N. A. Battista, A. J. Baird, and L. A. Miller, "A mathematical model and matlab code for muscle-fluid-structure simulations," Integr. Comp. Biol. **55**(5), 901–911 (2015).

[42] N. A. Battista, W. C. Strickland, and L. A. Miller, "IB2d: A Python and MATLAB implementation of the immersed boundary method," Bioinspir. Biomim. **12**(3), 036003 (2017).

[43] N. A. Battista, W. C. Strickland, A. Barrett, and L. A. Miller, "IB2d reloaded: A more powerful Python and MATLAB implementation of the immersed boundary method," Math. Methods Appl. Sci. **41**, 8455–8480 (2018).

[44] L. J. Fauci, "Peristaltic pumping of solid particles," Comput. Fluids **21**, 583–598 (1992).

[45] J. Du, R. D. Guy, and A. L. Fogelson, "An immersed boundary method for two-fluid mixtures," J. Comput. Phys. **262**, 231–243 (2014).

[46] J. Chrispell and L. Fauci, "Peristaltic pumping of solid particles immersed in a viscoelastic fluid," Math. Model. Nat. Phenom. **6**, 67–83 (2011).

[47] L. D. Waldrop and L. A. Miller, "Large-amplitude, short-wave peristalsis and its implications for transport," Biomech. Model. Mechanobiol. **15**, 629–642 (2016).

[48] W. Kou, J. E. Pandolfino, P. J. Kahrilas, and N. A. Patankar, "Simulation studies of the role of esophageal mucosa in bolus transport," Biomech. Model. Mechanobiol. **16**(3), 1001–1009 (2017).

[49] E. Jung and C. Peskin, "Two-dimensional simulations of valveless pumping using immersed boundary methods," SIAM J. Sci. Comput. **23**, 19–45 (2001).

[50] E. Jung, S. Lim, W. Lee, and S. Lee, "Computational models of valveless pumping using the immersed boundary method," Comput. Methods Appl. Mech. Eng. **197**, 2329–2339 (2008).

[51] W. Lee, E. Jung, and S. Lee, "Simulations of valveless pumping in an open elastic tube," SIAM J. Sci. Comput. **31**, 1901–1925 (2009).

[52] S. Lim and E. Jung, "Three-dimensional simulations of a closed valveless pump system immersed in a viscous fluid," SIAM J. Appl. Math. **70**, 1999–2022 (2010).

[53] S. J. Shin, C. B. Chang, and H. J. Sung, "Simulation of a valveless pump with an elastic tube," Int. J. Heat Fluid Flow **38**, 13–23 (2012).

[54] A. J. Baird, L. D. Waldrop, and L. A. Miller, "Neuromechanical pumping: Boundary flexibility and traveling depolarization waves drive flow within valveless, tubular hearts," Jpn. J. Indust. Appl. Math. **32**, 829–846 (2015).

[55] N. A. Battista and L. A. Miller, "Bifurcations in valveless pumping techniques from a coupled fluid-structure-electrophysiology model of heart development," BIOMATH **6**, 1711297 (2017).

[56] O. G. Ernst, A. Mugler, and H. S. E. Ullmann, "On the convergence of generalized polynomial chaos expansions," ESAIM: Math. Modell. Numer. Anal.. **46**, 317–339 (2012).

[57] M. Berveiller, B. Sudret, and M. Lemaire, "Stochastic finite element: A non intrusive approach by regression," Eur. J. Comput. Mech. **15**, 81–92 (2006).

[58] S. H. Jiang, D. Q. Li, and C. B. Zhou, "Optimal probabilistic collocation points for stochastic response surface method," Chin. J. Comput. Mech. **29**, 345–351 (2012).

[59] M. Taghizadeh, D. Xiu, and N. Alemazkoor, "Improving accuracy and computational efficiency of optimal design of experiments via greedy backward approach," Int. J. Uncertainty Quantif. **14**, 1–18 (2024).

[60] H. Niederreiter, *Random Number Generation and Quasi-Monte-Carlo Methods* (Society for Industrial and Applied Mathematics, Philadelphia, PA, 1992).

[61] M. Kuhn and K. Johnson, *Applied Predictive Modeling* (Springer, 2013), Vol. 26.

[62] A. Cozad, N. V. Sahinidis, and D. C. Miller, "Learning surrogate models for simulation-based optimization," AlChE. J. **60**, 2211–2227 (2014).

[63] X. Y. Zhang, M. Trame, L. Lesko, and S. Schmidt, "Sobol sensitivity analysis: A tool to guide the development and evaluation of systems pharmacology models," CPT. Pharmacom. Syst. Pharma. **4**, 69–79 (2015).

[64] A. Saltelli *et al.*, "Variance based sensitivity analysis of model output. Design and estimator for the total sensitivity index," Comp. Phys. Commun. **181**, 259–270 (2010).

[65] The College of New Jersey, Electronic Laboratory for Science & Analysis (ELSA) (2020), https://docs.hpc.tcnj.edu/ (accessed 24 January 2020).

[66] J. Ottesen, "Valveless pumping in a fluid-filled closed elastic tube-system: One-dimensional theory with experimental validation," J. Math. Biol. **46**, 309–332 (2003).

[67] A. Hickerson, D. Rinderknecht, and M. Gharib, "Experimental study of the behavior of a valveless impedance pump," Exp. Fluids **38**, 534–540 (2005).

[68] L. D. Waldrop, Y. He, N. A. Battista, T. N. Peterman, and L. A. Miller, "Uncertainty quantification reveals the physical constraints on pumping by peristaltic hearts," J. R. Soc. Inter. **17**, 2020032 (2020).

[69] Y. He, N. A. Battista, and L. D. Waldrop, "Mixed uncertainty analysis on pumping by peristaltic hearts using Dempster–Shafer theory," J. Math. Biol. **89**, 13 (2024).

[70] C. Ozalp, A. Pinarbasi, and B. Sahin, "Experimental measurement of flow past cavities of different shapes," Exp. Therm. Fluid Sci. **34**, 505–515 (2010).

[71] M. N. A. Saadun, M. Z. Sharudin, N. A. Che Sidik, and M. H. Mohd Hanafi, "Vortex formation for different geometry of cavities using high Reynolds number," in *Sustainable Energy and Development, Advanced Materials*, Applied Mechanics and Materials Vol. 699 (Trans Tech Publications Ltd, 2014), pp. 416–421.

[72] H. Asgharzadeh and I. Borazjani, "A non-dimensional parameter for classification of the flow in intracranial aneurysms. I. Simplified geometries," Phys. Fluids **31**, 031904 (2019).

[73] N. Hebdon, Y. He, and L. Waldrop, "*Getting best performance out of functional performance landscapes*" (*Authorea*, 2023).

[74] G. Bebis and M. Georgiopoulos, "Feed-forward neural networks," IEEE Potentials **13**, 27–31 (1994).

[75] X. Glorot and Y. Bengio, "Understanding the difficulty of training deep feedforward neural networks," in *Proceedings of the Thirteenth International Conference on Artificial Intelligence and Statistics*, Proceedings of Machine Learning Research Vol. 9, edited by Y. W. Teh and M. Titterington (PMLR, Chia Laguna Resort, Sardinia, Italy, 2010), pp. 249–256. https://proceedings.mlr.press/v9/glorot10a.html.

[76] P. Baldi and R. Vershynin, "The capacity of feedforward neural networks," Neural Netw. **116**, 288–311 (2019).

[77] K. Hornik, M. Stinchcombe, and H. White, "Multilayer feedforward networks are universal approximators," Neural Netw. **2**, 359–366 (1989).

[78] T. M. Russi, "Uncertainty quantification with experimental data and complex system models," Ph.D. thesis (UC Berkeley, 2010), pp. 1–158.

[79] P. G. Constantine, *Active Subspaces: Emerging Ideas for Dimension Reduction in Parameter Studies* (SIAM, Philadelphia, PA, 2015).

[80] T. W. Lukaczyk, P. Constantine, F. Palacios, and J. J. Alonso, *Active Subspaces for Shape Optimization* (American Institute of Aeronautics and Astronautics, 2014), pp. 1–18.

[81] G. Boncoraglio, C. Farhat, and C. Bou-Mosleh, "Model reduction framework with a new take on active subspaces for optimization problems with linearized fluid-structure interaction constraints," Int. J. Numer. Methods Eng. **122**, 5450–5481 (2021).

[82] R. A. Bridges, A. D. Gruber, C. Felder, M. Verma, and C. Hoff, "Active manifolds: A non-linear analogue to active subspaces" (2019), https://arxiv.org/abs/1904.13386 (accessed 03 June 2022).

[83] R. R. Lam, O. Zahm, Y. M. Marzouk, and K. E. Willcox, "Multifidelity dimension reduction via active subspaces," SIAM J. Sci. Comput. **42**, A929–A956 (2020).

[84] N. Wycoff, M. Binois, and S. M. Wild, "Sequential learning of active subspaces," J. Comput. Graphical Stat. **30**, 1224–1237 (2021).

[85] D. Khatamsaz *et al.*, "Adaptive active subspace-based efficient multifidelity materials design," Mater. Des. **209**, 110001 (2021).

[86] P. G. Constantine and P. Diaz, "Global sensitivity metrics from active subspaces," Rel. Eng. Syst. Safety **162**, 1–13 (2017).

[87] C. S. Peskin, "The immersed boundary method," Acta Numerica **11**, 479–517 (2002).